ALTERNATIVE METHODOLOGIES FOR BORESIGHT CALIBRATION OF GNSS/INS-ASSISTED PUSH-BROOM HYPERSPECTRAL SCANNERS ON UAV PLATFORMS

by

Tian Zhou

A Thesis

Submitted to the Faculty of Purdue University

In Partial Fulfillment of the Requirements for the degree of

Master of Science in Civil Engineering

Lyles School of Civil Engineering

West Lafayette, Indiana

May 2019

THE PURDUE UNIVERSITY GRADUATE SCHOOL

STATEMENT OF COMMITTEE APPROVAL

Dr. Ayman Habib, Chair

Lyles School of Civil Engineering

Dr. Melba Crawford

Lyles School of Civil Engineering

Dr. James Bethel

Lyles School of Civil Engineering

Approved by:

Dr. Dulcy Abraham

Head of the Graduate Program

To my parents

ACKNOWLEDGMENTS

First and foremost, I would like to express my sincere gratitude to my advisor Dr. Ayman Habib for all his guidance and supports during my graduate studies. I have been extremely lucky to have a supervisor who cared so much about my work, and who responded to my questions and queries so promptly. Without his valuable suggestions on my research and providing excellent study environment, this dissertation would not have been possible. Besides my advisor, I would like to thank the rest of my thesis committee: Dr. Melba Crawford, and Dr. James Bethel for their insightful comments and encouragement, but also for the hard question which incented me to widen my research from various perspectives.

I would also express my gratitude to my colleagues at the Digital Photogrammetry Research Group and Advance Research Projects Agency-Energy team, Ali Masjedi, Evan Flatt, Zhou Zhang, Fangning He, Radhika Ravi, Yun-Jou Lin, Seyyed Hasheminasad, Magdy Elbahnasawy, Tamer Shamseldin, and Weifeng Xiong.

In addition, I deeply thank my dear parents for their unconditional trust, timely encouragement, and endless patience.

Finally, I would like to acknowledge the financial support from the Department of Energy. The information, data, or work presented herein was funded in part by the Advanced Research Projects Agency-Energy (ARPA-E), U.S. Department of Energy, under Award Number DE-AR0000593. The views and opinions of authors expressed herein do not necessarily state or reflect those of the United States Government or any agency thereof.

TABLE OF CONTENTS

LIST OF TABLES

LIST OF FIGURES

ABBREVIATIONS

ACRE	Agronomy Center for Research and Education
DEM	digital elevation model
DLT	direct linear transformation
GCP	ground control point
GNSS	global navigation satellite systems
GSD	ground sampling distance
IMU	inertial measurement unit
INS	inertial navigation systems
LSA	least squares adjustment
MMS	mobile mapping system
RMSE	root mean square error
SURF	speeded up robust feature
STD	standard deviation
UAV	unmanned aerial vehicle

ABSTRACT

Author: Tian, Zhou. MSCE
Institution: Purdue University
Degree Received: May 2019
Title: Alternative Methodologies for Boresight Calibration of GNSS/INS-Assisted Push-Broom Hyperspectral Scanners on UAV Platforms
Major Professor: Ayman Habib

Low-cost unmanned aerial vehicles (UAVs) utilizing push-broom hyperspectral scanners are poised to become a popular alternative to conventional remote sensing platforms such as manned aircraft and satellites. In order to employ this emerging technology in fields such as high-throughput phenotyping and precision agriculture, direct georeferencing of hyperspectral data using onboard integrated global navigation satellite systems (GNSS) and inertial navigation systems (INS) is required. Directly deriving the scanner position and orientation requires the spatial and rotational relationship between the coordinate systems of the GNSS/INS unit and hyperspectral scanner to be evaluated. The spatial offset (lever arm) between the scanner and GNSS/INS unit can be measured manually. However, the angular relationship (boresight angles) between the scanner and GNSS/INS coordinate systems, which is more critical for accurate generation of georeferenced products, is difficult to establish. This research presents three alternative calibration approaches to estimate the boresight angles relating hyperspectral push-broom scanner and GNSS/INS coordinate systems. For reliable/practical estimation of the boresight angles, the thesis starts with establishing the optimal/minimal flight and control/tie point configuration through a bias impact analysis starting from the point positioning equation. Then, an approximate calibration procedure utilizing tie points in overlapping scenes is presented after making some assumptions about the flight trajectory and topography of covered terrain. Next, two rigorous approaches are introduced – one using Ground Control Points (GCPs) and one using tie

points. The approximate/rigorous approaches are based on enforcing the collinearity and coplanarity of the light rays connecting the perspective centers of the imaging scanner, object point, and the respective image points. To evaluate the accuracy of the proposed approaches, estimated boresight angles are used for ortho-rectification of six hyperspectral UAV datasets acquired over an agricultural field. Qualitative and quantitative evaluations of the results have shown significant improvement in the derived orthophotos to a level equivalent to the Ground Sampling Distance (GSD) of the used scanner (namely, 3-5 cm when flying at 60 m).

1. INTRODUCTION

1.1 Background

In many of today's rapidly growing technological and industrial fields, hyperspectral imaging is quickly emerging as an irreplaceable mechanism for collecting high-quality scientific data. For each pixel in the scene, the spectrum is obtained by measuring radiance in contiguous spectral bands with fine wavelength resolution. By measuring the spectral radiance in narrow bands across large swaths of the electromagnetic spectrum, hyperspectral sensors, or imaging spectrometers, are able to provide large amounts of characteristic information pertaining to the objects they capture. Thus, the continuous spectrum can be adopted to characterize the objects in the scene with great precision and detail. Compared to a conventional RGB camera, which only acquires three different spectral channels corresponding to the visual primary colors, hyperspectral imaging leads to a massively improved ability to classify and analyze the objects based on their spectral properties.

The growing popularity of hyperspectral imaging technology and recent advances in UAVs created an environment where high resolution hyperspectral imaging is more accessible than ever. Hyperspectral imaging has been adopted to a considerable extent in precision agricultural applications [1], [2]. Crop monitoring for nutrients, disease, insect attack, and overall plant health is essential to ensure successful agricultural operations. Previously, this task was achieved mainly by visual examination of crops either from ground or from sky. However, due to the limited ability of human eye to detect the crop condition, this traditional method no longer fulfills the requirements for precision agriculture. Modern precision agriculture aims to maximize yield and resources while reducing the environmental impacts using site-specific management tactics.

Phenotypic data are widely used to improve management of farm inputs such as fertilizers, herbicides, seed, and fuel [3]. Phenotypic data captured by hyperspectral sensors enables researchers and agronomists to sense crop characteristics such as moisture content, nutrients, chlorophyll, leaf area index, and crop biomass without the drawbacks associated with laborious and expensive in-field measurements [4].

In the past, hyperspectral imaging utilized Mobile Mapping Systems (MMS), such as satellites and manned aircrafts as the platforms for agricultural data collection. Modern MMS including terrestrial and airborne platforms provide economic and accurate means to collect data for urban mapping, environmental monitoring, transportation planning, change detection, resource management, and precision agriculture [5]. Due to recent improvements in the accuracy of integrated GNSS and INS, MMS can now provide georeferenced data with high spatial accuracy. The utilization of GNSS and INS has not only increased the efficiency of mobile mapping considerably, but has also resulted in greater flexibility and lower cost. For agricultural management applications, the increased requirements for geospatial data at a higher spatial resolution and temporal frequency made it clear that manned aircraft and satellite remote sensing systems cannot fully satisfy such needs.

Therefore, low-cost UAVs are emerging as ideal alternative platforms for agricultural management [6]. UAVs offer several design and performance advantages over other conventional platforms, such as small size, low weight, low flying height, slow flight speed, low cost, and ease of storage and deployment [7], [8]. A UAV-based MMS is capable of providing high spatial resolution data (e.g., centimeter-level GSD) at a higher data collection rate (e.g., daily acquisitions). Meanwhile, integrated GNSS/INS mounted on a UAV allows for directly georeferencing the acquired data with high accuracy while eliminating the need for an excessive number of GCPs.

Thus, UAVs could be an inexpensive and more practical substitute for satellites and general aviation aircrafts for the acquisition of high resolution remotely sensed data for agriculture applications.

Due to the large volume of acquired data by a hyperspectral scanner, high spatial resolution systems are usually based on having a 1-D array along the focal plane while operating through what is commonly known as a "push-broom scanning mechanism". A push-broom scanner, which uses a linear array of optical spectroscopic units that are perpendicular to the moving direction, acquires a thin image at a given exposure. To obtain full coverage of a mapping area, a scene is formed by successive exposures along the flight trajectory and concatenating the acquired images [9].

In terms of frame hyperspectral sensors, a 2-D footprint is captured in a single exposure. A frame sensor has a narrower swath width and requires more optical sensing units [10]. The difference between push-broom imaging and frame imaging is shown in Figure 1.1. Since the frame imagery is directly captured by a 2-D CCD/CMOS array in a frame camera, it has better internal geometry [11]. However, the frame imaging sensor requires more CCD/CMOS detectors than push-broom scanner. In addition, for frame hyperspectral sensor, the different spectral channels may not be sensed simultaneously [12]. Thus, push-broom sensors encompassing the visible, near-infrared (NIR), and shortwave infrared (SWIR) bands of the EM spectrum have been traditionally used in hyperspectral imaging.

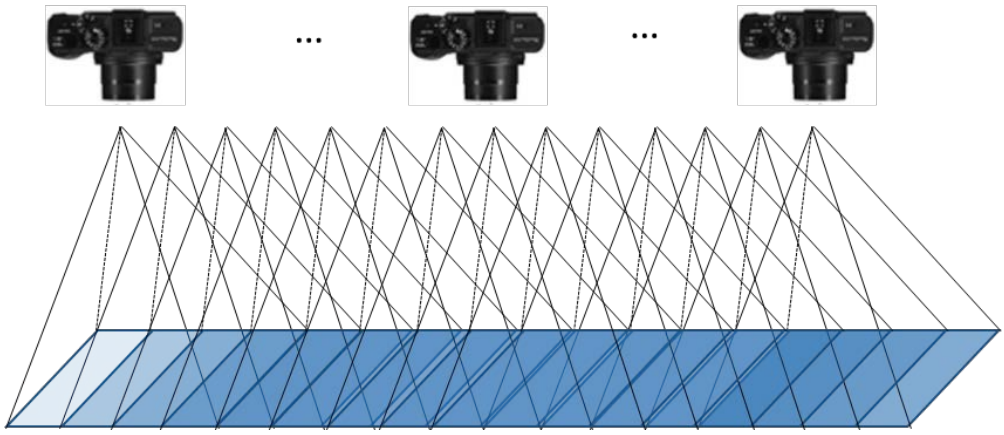

(a)

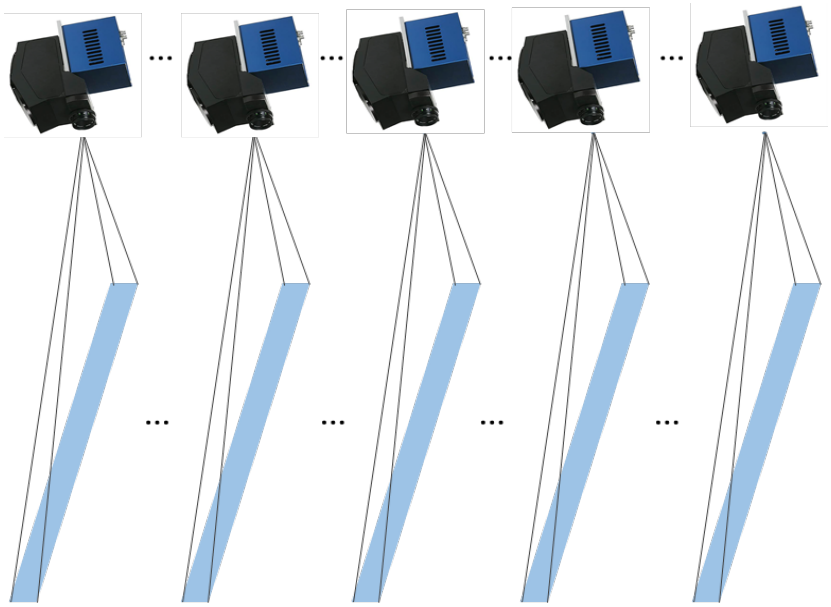

(b)

Figure 1.1: Comparison of (a) frame sensor and (b) push-broom sensor

1.2 Motivation and Problem Statement

In order to derive accurate 3D geospatial information from 2D hyperspectral scenes, the interior and exterior orientation of the utilized sensor should be established. Interior orientation, which

encompasses the internal sensor characteristics such as focal length and lens distortion, is established through a sensor calibration procedure. Exterior orientation, which defines the position and orientation of the scanner at the moment of exposure, is traditionally established through indirect georeferencing by using a series of precisely surveyed and well-distributed GCPs in the bundle adjustment procedure. Nowadays, with the help of an integrated GNSS/INS unit onboard, the exterior orientation parameters can be directly estimated without the need for GCPs [13–15]. Indirect georeferencing is able to provide accurate triangulation results; however, employing GCPs is very costly. On the other hand, direct geo-referencing offers a great opportunity for more efficient and economical mapping applications by reducing the time and expense, but its accuracy highly depends on the grade of the direct geo-referencing GNSS/INS unit, as well as the stability of system calibration procedure.

Considering that the exterior orientation parameters of every scan line have to be determined, a direct georeferencing procedure is usually adopted to provide the position and orientation of the scanner using an integrated GNSS/INS unit. In this regard, one should note that the GNSS/INS position and orientation refer to the body frame of the Inertial Measurement Unit (IMU). Therefore, the lever arm components and boresight angles between the hyperspectral push-broom scanner and IMU body frame coordinate systems need to be estimated to derive accurate position and orientation of the scanner. The lever arm denoting the spatial displacement between the IMU body frame and the perspective center of the scanner can be established to a reasonable accuracy (e.g., 2-3 cm) using conventional measurements tools [16]. However, boresight angles relating the IMU body frame and the scanner coordinate systems can only be roughly established. The boresight angles play more critical role than the lever arm components in controlling the geospatial accuracy of derived products due to the error propagation of the former with the platform height. Thus,

reliable boresight angles calibration is essential for ensuring the spatial accuracy of GNSS/INS-assisted imaging platforms. To date, a great deal of research has been conducted on boresight calibration for frame imaging sensors. However, in terms of push-broom scanners, reliable boresight calibration still remains to be addressed especially when the scanner is implemented onboard a UAV mapping platform.

1.3 Thesis Outline

The remainder of this thesis explains the proposed alternative boresight calibration strategies of GNSS/INS-assisted push-broom hyperspectral scanners in more details as explained below:

- Existing pertinent research for boresight calibration is reviewed in Chapter 2.
- The optimal/minimal configuration of the flight and control/tie point layout for reliable/practical boresight calibration is investigated through bias impact analysis in Chapter 3.
- In Chapter 4, an approximate approach that starts with the outcome of the bias impact analysis is introduced for evaluating the boresight angles using tie points in overlapping scenes. Then, two rigorous approaches, which use GCPs and tie points, are presented.
- Experimental results from several real datasets are presented in Chapter 5 to verify the feasibility of the proposed approaches.
- Finally, the advantages and disadvantages of the presented approaches are listed and recommendations for future work are provided in Chapter 6.

2. RELATED WORK

2.1 Overview

As has been introduced in Chapter 1, boresight calibration approaches of frame imaging sensors through bundle adjustment of overlapping images along and across the flight direction together with several GCPs are well-established [17–19]. Therefore, the existing pertinent boresight calibration strategies for push-broom scanners are discussed in this chapter.

2.2 Boresight Calibration of Push-Broom Scanner

For push-broom scanners, significant research has been dedicated towards establishing reliable boresight calibration strategies. Muller *et al.* [20] proposed a boresight calibration approach for airborne and space borne push-broom scanners. In this approach, the boresight angles were estimated by minimizing the difference between the ground coordinates of GCPs and the projected ground coordinates of the respective image points based on the collinearity concept. More specifically, using the interior orientation parameters, GNSS/INS georeferencing parameters, nominal lever arm components and boresight angles, and an available Digital Elevation Model (DEM), the image points corresponding to established GCPs were projected onto the DEM using a ray tracing procedure. Then, boresight angles were estimated by minimizing the differences between the GCPs and the projected ground coordinates. The experimental dataset in this work was acquired by the push-broom scanner "ROSIS-03" over a test site from a flying height of 3,230m. An IGI AeroControl CCNS IIb was used for the determination of platform position and orientation. The accuracy of the GNSS/INS position and orientation information is about 0.1-0.3

m and 0.01°-0.1°, respectively. Using a DEM with 5-10 m vertical accuracy and 25 m horizontal resolution, 5 GCPs were used for boresight calibration. The estimated ground coordinates of 7 check points were compared to the surveyed coordinates to evaluate the accuracy of the boresight calibration procedure. The root mean square error (RMSE) of the differences in the XY-coordinates was around 1.5 m, which is almost at the same level as the GSD of the used sensor (1.9 m).

Based on the conceptual basis of the approach proposed by Muller *et al.* [20], similar strategies involving additional parameters (e.g., aircraft stabilizer scaling factors and variations of sensor's CCD size) in the calibration procedure were discussed in Yeh and Tsai [21] and Zhang *et al.* [22]. Yeh and Tsai [21] adopted 19 self-calibration parameters in the direct georeferencing procedure for rectifying airborne push-broom hyperspectral images: (1) the lever arm components and boresight angles between the hyperspectral push-broom scanner and IMU body frame coordinate systems; (2) scaling factors of the stabilizer (stabilizer is adopted to reduce the vibration and rotation of the aircraft); (3) scaling factor variation of the sensor's CCD size in the column direction; and (4) interior orientation parameters of the sensor's optical system, including focal length, offsets of the principal point, and the distortion parameters. These parameters were estimated by iterative least square adjustment using a set of well-distributed GCPs. Two experimental image sets along with the GNSS/INS data and 40 GCPs were used to solve these parameters using 30 check points. The ground coordinates of the GCPs and check points were surveyed by GNSS receiver through a Real-time kinematic positioning procedure with an accuracy of 0.02 m in horizontal direction and an accuracy of 0.05 m in vertical direction. When flying at 2000 m height, the corresponding GSD is about 1.9 m. Rectified image was generated using the estimated 19 parameters, and the positional errors of the 40 GCPs points were significantly reduced

to 2.9 m and 2.6 m (GSD level) from 28.2 m and 18.8 m before rectification. And similar results were found for the check points. Zhang *et al.* [22] considered the drift error of the exterior orientation parameters derived from GNSS/INS system to improve the accuracy of estimating boresight angles. The exterior parameters were made up of the position and orientation measured by GNSS/INS system and the drift errors. This approach was demonstrated through both simulated data and real dataset. The achieved geometric accuracy for the ortho-rectified mosaics using the estimated boresight angles was found to be accurate at the level of the GSD of the involved sensors.

Lenz *et al.* [23] proposed an automated in-flight boresight calibration approach for push-broom scanners. The boresight angles were estimated by forcing conjugate light rays to intersect as well as possible. The proposed strategy applied speeded up robust feature (SURF) detector to identify interest points, whose descriptors were used in a matching routine to derive homologous points in overlapping scenes. Then, tie points were projected onto a DEM utilizing a ray tracing algorithm using nominal values for the boresight angles. The boresight angles were derived by minimizing the root mean square error between the ground coordinates of corresponding tie points. The approach was evaluated using two datasets with overlapping strips over a forested mountain and a relatively flat urban area, where the average GSD was 0.5 m for both datasets. To evaluate the boresight calibration results, residual errors were calculated using a reference dataset comprised of manually defined tie points. The RMSE of the residual errors was 1.5 m (three times the GSD) for the forest dataset and 0.5 m (GSD level) for the urban area.

Instead of estimating boresight angles directly, Habib *et al.* [8] focused on mitigating the impact of boresight errors and residual errors in the direct geo-referencing information through a registration procedure. Due to the better internal geometry of frame sensor, RGB-based orthophotos are used to improve the geometric quality of partially-rectified hyperspectral

orthophotos contaminated by the impact of residual errors in the direct geo-referencing information. First, the transformation function relating the reference frames of the RGB-based and partially rectified hyperspectral orthophotos as a result of residual errors in the direct georeferencing information was established based on the collinearity equations. Then, geometric primitives, which are mainly linear features, were identified in both RGB-based and partially rectified hyperspectral orthophotos to derive involved parameters in the transformation function. In order to reduce the number of involved transformation parameters, reference points along the columns of the partially rectified hyperspectral orthophoto were established. Transformation parameters at a given time were estimated by interpolation of the respective transformation parameters associated with neighboring reference points. The performance of the proposed approach was verified through real datasets that have been collected over an agricultural field. Tie points, linear features, and reference points were manually established in the experiments. The average GSD was 5 cm for hyperspectral data, and the geometric accuracy of generated partially-rectified hyperspectral orthophoto was in the range of ±5 m. In terms of RGB data, the quality of orthophoto mosaic of the entire test field was in the range of ±4 cm. The quality of fit between the RGB-based features and their transformed counterparts in the hyperspectral orthophoto qualitatively indicated the success of the registration process. For quantitative evaluation of the registration quality, the registration procedure reduced the quality of fit between tie and check features from roughly ±2.5 m to almost ±0.25 m.

2.3 Conclusions

The key limitation of the above approaches is the need for having a DEM of the covered area as well as some GCPs. As for the registration approach proposed by Habib *et al.*, the boresight angles

were not estimated directly. Moreover, none of the previous literature addressed the optimal/minimal flight and control/tie point configuration for reliable estimation of the boresight angles. In response to these limitations, this thesis starts with an investigation of the optimal/minimal configuration of the flight and control/tie point layout for reliable/practical boresight calibration through bias impact analysis. The analysis is based on evaluating the impact of incremental changes in the boresight pitch, roll, and heading angles ($\delta\Delta\omega$, $\delta\Delta\varphi$, and $\delta\Delta\kappa$) on derived ground coordinates after making some assumptions regarding the flight trajectory and topography of the covered terrain (e.g., parallel scanner and IMU coordinate systems and vertical scanner over relatively flat/horizontal terrain). The derived impact is then used to establish an optimal/minimal flight and control/tie point configuration for reliable boresight angles estimation.

3. BIAS IMPACT ANALYSIS FOR BORESIGHT ANGLES

3.1 Overview

As discussed in the Chapter 2, the boresight angles for a GNSS/INS-assisted push-broom scanner are usually determined with the help of a DEM together with a set of GCPs. In this research, the boresight angles will be determined using either a set of GCPs or tie points that are manually identified in overlapping push-broom scanner scenes. When using GCPs, the boresight estimation strategy aims at ensuring the collinearity of the GCP, corresponding image point, and perspective center of the scan line encompassing the image point. When relying on tie points, the boresight angle estimation strategy enforces precise intersection of the light rays connecting the perspective centers of the scan lines encompassing corresponding image points of the tie points and the respective conjugate image points. In other words, the calibration target function aims at estimating the boresight angles that ensures the best intersection of light rays connecting the perspective centers and conjugate image points.

An optimal flight and control/tie point configuration is the one that will exhibit large deviations from the respective target functions (i.e., collinearity or coplanarity) due to small changes in the boresight angles. Therefore, the optimal flight and control/tie point configuration can be set only after analyzing the impact of biases in the boresight angles on the collinearity/coplanarity target functions. Such bias impact can be established by considering the collinearity equations and evaluating the changes in the ground coordinates of derived object points as a result of biases in the boresight angles. Evaluating the bias impact on derived ground coordinates is directly related to the GCP-based approach since the bias impact will violate the collinearity objective. On the other hand, the impact on the ground coordinates is indirectly related to the tie points-based approach since the bias impact on the ground coordinates will also cause deviations from the

coplanarity of corresponding light rays associated with the image points for the tie point in question.

In this chapter, first, the mathematical model of the collinearity principle is introduced. Based on the collinearity equations, the impact of incremental changes in the boresight angles on derived ground coordinates is evaluated. The derived impact is then used to establish an optimal/minimal flight and control/tie point configuration for reliable boresight angles estimation.

3.2 Point Positioning Equations

The developed strategies for bias impact analysis and boresight calibration are based on the collinearity equations, which describe the conceptual basis of point positioning using GNSS/INS-assisted push-broom scanners. A push-broom scanner system involves three coordinate systems – a mapping frame, an IMU body frame, and a scanner frame. The mathematical model of the collinearity principle – which describes the collinearity of the scanner perspective center, image point, and corresponding object point – is graphically illustrated and mathematically introduced in Figure 3.1 and Equation 3.1, respectively.

$$r_l^m = r_b^m(t) + R_b^m(t) r_c^b + \lambda_i R_b^m(t) R_c^b r_i^c \tag{3.1}$$

The notations for spatial vectors and rotations used in Figure 3.1 and Equation 3.1 are as follows: i) $\boldsymbol{r_a^b}$ denotes the spatial offset for point $\boldsymbol{a}$ relative to a coordinate system associated with point $\boldsymbol{b}$; ii) $\boldsymbol{R_a^b}$ denotes the rotation matrix that transforms a vector from coordinate system $\boldsymbol{a}$ to coordinate system $\boldsymbol{b}$. The superscripts/subscripts $\boldsymbol{m}$, $\boldsymbol{b}$, and $\boldsymbol{c}$ represent the mapping, IMU body frame, and camera/scanner coordinate systems, respectively. In Equation 3.1, $\boldsymbol{r_l^m}$ represents ground

coordinates of the object point $\boldsymbol{I}$; $\boldsymbol{r_b^m(t)}$ and $\boldsymbol{R_b^m(t)}$ are the GNSS/INS-based position and orientation information of the IMU body frame coordinate system relative to the mapping frame; $\boldsymbol{r_c^b}$ and $\boldsymbol{R_c^b}$ are the lever-arm vector and boresight rotation matrix relating the push-broom scanner and IMU body frame coordinate systems; $\boldsymbol{r_i^c}$ denotes the vector connecting the scanner perspective center to the image point, $\boldsymbol{i}$, corresponding to an object point, $\boldsymbol{I}$; and $\boldsymbol{\lambda_i}$ is a point-specific unknown scale factor that varies with the terrain relief and scanner tilt. As illustrated in Figure 3.1, one can define the xyz-axes of the scanner coordinate system to be aligned across flight, along flight, and up directions, respectively. In the case of push-broom scanners, the y-image coordinates for any point would be constant, which depends on the scanner alignment along the focal plane. Usually, the scan line is set vertically below the perspective center of the used lens – thus making the y-image coordinate almost zero. The y-scene coordinate defines the exposure time for the scan line in question, as shown in Figure 3.2. Starting with Equation 3.1, one can perform the boresight bias impact analysis for a push-broom scanner.

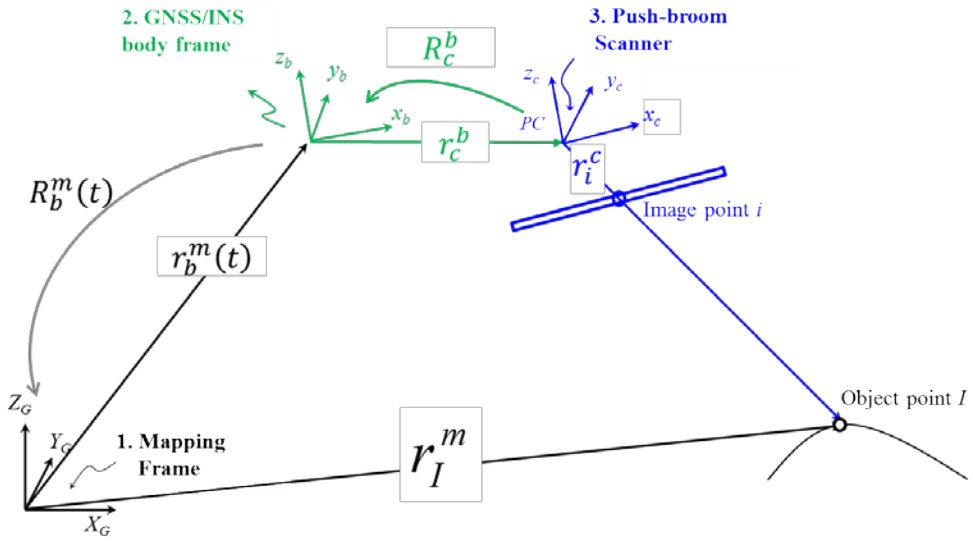

Figure 3.1: Schematic diagram of the collinearity equations and definition of the coordinate systems for a push-broom scanner

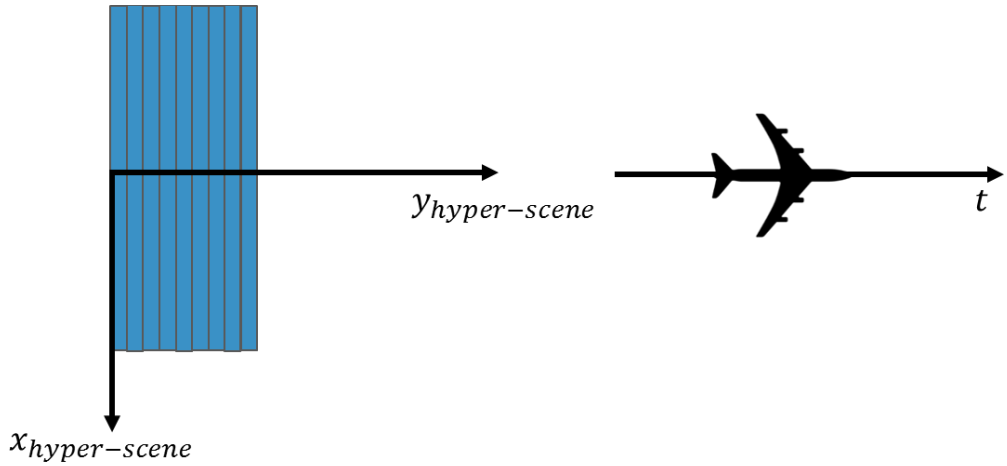

Figure 3.2: Coordinate system ($x_{hyper-scene}$, $y_{hyper-scene}$) for a hyperspectral scene

3.3 Bias Impact Analysis

To facilitate straightforward analysis of the bias impact, we will make some assumptions regarding the system setup, flight trajectory, and topography of the covered area. More specifically, we will be making the following assumptions:

1) The IMU is setup in the platform with its x, y, and z-axes pointing in the starboard, forward, and up directions, respectively.
2) The z-axis of IMU coordinate system is aligned along the vertical direction (i.e., the ω and φ angles of the $\boldsymbol{R_b^m(t)}$ rotation matrix are zeros).
3) The platform is traveling in the *South-to-North* (denoted as *forward*) and *North-to-South* (denoted as *backward*) directions while maintaining a constant heading. Thus, the κ angles for the *forward* and *backward* directions will be 0° and 180°, respectively.
4) The push-broom scanner coordinate system is almost parallel to the IMU body frame (i.e., the angular offsets between these coordinate systems – $\Delta\omega, \Delta\varphi$, and $\Delta\kappa$ – are within ±5°), as shown in Figure 3.3.

5) The push-broom scanner is flying at a constant elevation while covering a relatively flat terrain.

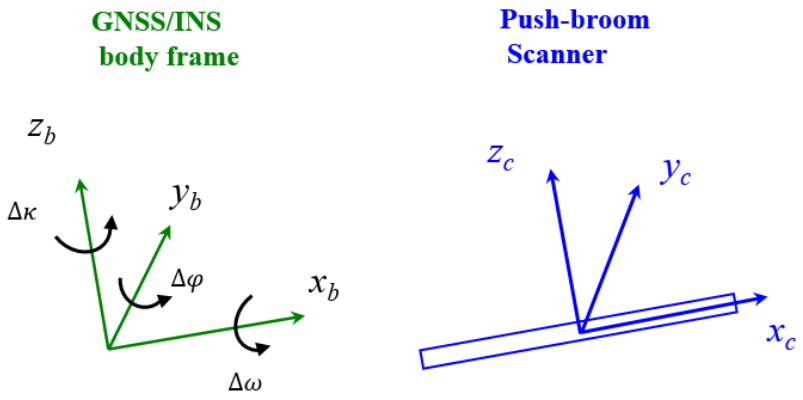

Figure 3.3: Alignment of the scanner and IMU body frame coordinate systems

Assumptions 2 and 3 would result in $\boldsymbol{R_b^m(t)}$ being defined according to Equation 3.2, where the top and bottom signs refer to the *forward* and *backward* flight directions, respectively. Assumption 4 would lead to a boresight matrix R_c^b that is defined by the incremental rotation in Equation 3.3, where $\Delta\omega, \Delta\varphi$, and $\Delta\kappa$ represent the boresight pitch, roll, and heading angles (as shown in Figure 3.3), respectively.

$$R_b^m(t) = \begin{bmatrix} \pm 1 & 0 & 0 \\ 0 & \pm 1 & 0 \\ 0 & 0 & 1 \end{bmatrix} \tag{3.2}$$

$$R_c^b = \begin{bmatrix} 1 & -\Delta\kappa & \Delta\varphi \\ \Delta\kappa & 1 & -\Delta\omega \\ -\Delta\varphi & \Delta\omega & 1 \end{bmatrix} \tag{3.3}$$

One should note that the above assumptions are only introduced to facilitate the bias impact analysis. The findings of the analysis would still apply regardless of the flight directions, IMU alignment, push-broom scanner alignment relative to the IMU body frame, flying height variation, and nature of covered terrain unless it is explicitly stated in the forthcoming boresight angles

estimation strategies.

Following the above assumptions, the point positioning equation for a push-broom scanner would reduce to the form in Equations 3.4-3.6 (with f being the focal length), where once again the top and bottom signs refer to the *forward* and *backward* flight directions, respectively.

$$r_I^m = r_b^m(t) + \begin{bmatrix} \pm\Delta X \\ \pm\Delta Y \\ \Delta Z \end{bmatrix} + \lambda_i \begin{bmatrix} \pm 1 & 0 & 0 \\ 0 & \pm 1 & 0 \\ 0 & 0 & 1 \end{bmatrix} \begin{bmatrix} 1 & -\Delta\kappa & \Delta\varphi \\ \Delta\kappa & 1 & -\Delta\omega \\ -\Delta\varphi & \Delta\omega & 1 \end{bmatrix} \begin{bmatrix} x_i \\ 0 \\ -f \end{bmatrix} \tag{3.4}$$

$$r_I^m = r_b^m(t) + \begin{bmatrix} \pm\Delta X \\ \pm\Delta Y \\ \Delta Z \end{bmatrix} + \lambda_i \begin{bmatrix} \pm 1 & \mp\Delta\kappa & \pm\Delta\varphi \\ \pm\Delta\kappa & \pm 1 & \mp\Delta\omega \\ -\Delta\varphi & \Delta\omega & 1 \end{bmatrix} \begin{bmatrix} x_i \\ 0 \\ -f \end{bmatrix} \tag{3.5}$$

$$r_I^m = r_b^m(t) + \begin{bmatrix} \pm\Delta X \\ \pm\Delta Y \\ \Delta Z \end{bmatrix} + \lambda_i \begin{bmatrix} \pm x_i \mp f\Delta\varphi \\ \pm x_i\Delta\kappa \pm f\Delta\omega \\ -x_i\Delta\varphi - f \end{bmatrix} \tag{3.6}$$

In Equations 3.4-3.6, $[\Delta X \quad \Delta Y \quad \Delta Z]^T$ represents the lever arm vector relating the IMU body frame and scanner while $[x_i \quad 0 \quad -f]^T$ represents the vector $\boldsymbol{r_i^c}$ connecting the perspective center and the image point in question. Using Equation 3.6, one can derive the impact of a bias in the boresight angles on the ground coordinates of the derived object point through partial derivatives w.r.t. the boresight pitch, roll, and heading angles and its multiplication with assumed biases (namely, $\delta\Delta\omega$, $\delta\Delta\varphi$, and $\delta\Delta\kappa$). Before proceeding with such analysis, one should note that owing to the push-broom scanning mechanism, a variation in the boresight roll angle ($\Delta\varphi$) will result in a tilt of the scan line relative to the covered terrain, thus leading to a variation in the scale factor ($\boldsymbol{\lambda_i}$) along the scan line, as shown in Figure 3.4. Alternatively, variations in boresight pitch ($\Delta\omega$) and boresight heading ($\Delta\kappa$) angles will not affect the scale factor as the scan line would still remain parallel to the terrain. Therefore, the dependency of the scale factor ($\boldsymbol{\lambda_i}$) on the boresight roll angle ($\Delta\varphi$) should be considered within the bias impact analysis.

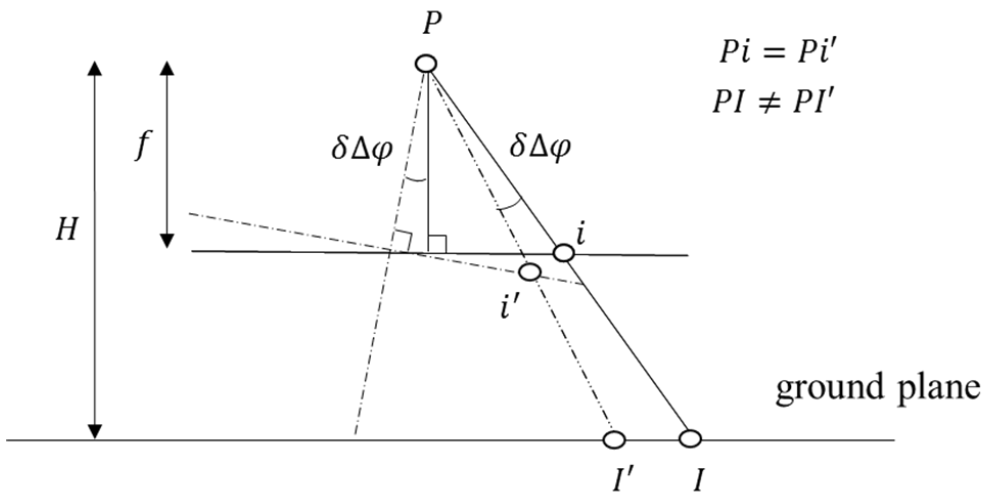

Figure 3.4: Impact of variation in the boresight roll angle (δΔφ) on the scale factor λ_i for a push-broom scanner

Starting with the simplified collinearity, Equation 3.6, the impact of variation in the boresight pitch angle ($\delta\Delta\omega$) can be presented by Equation 3.7, where the scale factor is approximated as $\lambda_i = \frac{H}{f}$, owing to the assumption of having a vertical scanner over relatively flat terrain.

$$\delta r_I^m(\delta\Delta\omega) = \lambda_i \begin{bmatrix} 0 \\ \pm f\delta\Delta\omega \\ 0 \end{bmatrix} = \begin{bmatrix} 0 \\ \pm H\delta\Delta\omega \\ 0 \end{bmatrix} \tag{3.7}$$

Similarly, the impact of variation in the boresight heading angle (δΔκ) can be given by Equation 3.8. $\boldsymbol{X_I'}$ in Equation 3.8 represents the lateral distance, while considering the appropriate sign, between the object point and the flight trajectory.

$$\delta r_I^m(\delta\Delta\kappa) = \lambda_i \begin{bmatrix} 0 \\ \pm x_i\delta\Delta\kappa \\ 0 \end{bmatrix} = \begin{bmatrix} 0 \\ \pm X_I'\delta\Delta\kappa \\ 0 \end{bmatrix} \tag{3.8}$$

where $X_I' = \lambda_i x_i \approx \frac{H}{f} x_i$

One should note that for a given object point, $\boldsymbol{x_i}$ and $\boldsymbol{X_I'}$ will change their sign depending on the flying direction, as shown in Figure 3.5.

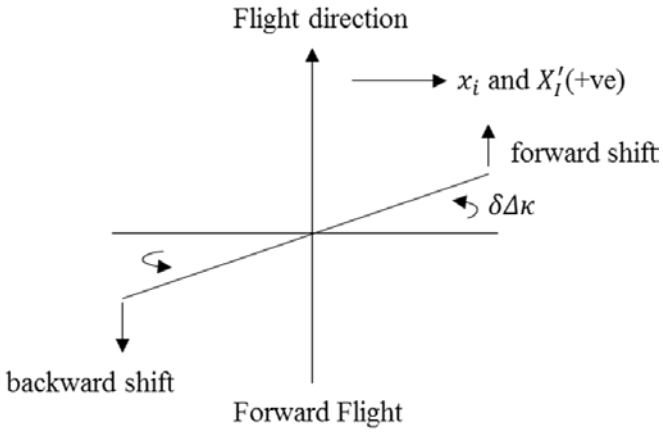

(a)

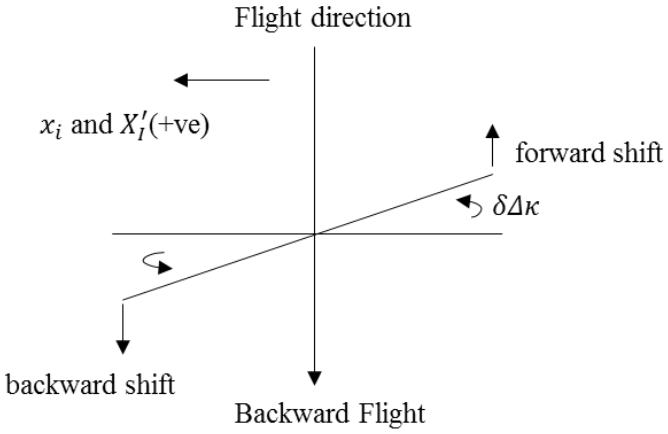

(b)

Figure 3.5: Impact of variation in the boresight heading angle on ground coordinates

For the impact of variation in the boresight roll angle ($\delta\Delta\varphi$), one should also consider the impact of such variation on the scale factor. Thus, the combined impact on the ground coordinates can be represented by Equation 3.9, which, in turn, could be expanded to Equation 3.10 (after replacing $\frac{\partial\lambda_i}{\partial\Delta\varphi}\delta\Delta\varphi$ with $\delta\lambda_i(\delta\Delta\varphi)$).

$$\delta r_I^m(\delta\Delta\varphi) = \lambda_i \begin{bmatrix} \mp f\delta\Delta\varphi \\ 0 \\ -x_i\delta\Delta\varphi \end{bmatrix} + \frac{\partial\lambda_i}{\partial\Delta\varphi}\delta\Delta\varphi \begin{bmatrix} \pm x_i \mp f\Delta\varphi \\ \pm x_i\Delta\kappa \pm f\Delta\omega \\ -x_i\Delta\varphi - f \end{bmatrix} \tag{3.9}$$

$$\delta r_I^m(\delta\Delta\varphi) = \lambda_i \begin{bmatrix} \mp f\delta\Delta\varphi \\ 0 \\ -x_i\delta\Delta\varphi \end{bmatrix} + \begin{bmatrix} \pm x_i\,\delta\lambda_i(\delta\Delta\varphi) \mp \boldsymbol{f\,\Delta\varphi\,\delta\lambda_i(\delta\Delta\varphi)} \\ \pm\boldsymbol{x_i\,\Delta\kappa\,\delta\lambda_i(\delta\Delta\varphi)} \pm \boldsymbol{f\,\Delta\omega\,\delta\lambda_i(\delta\Delta\varphi)} \\ -\boldsymbol{x_i\,\Delta\varphi\,\delta\lambda_i(\delta\Delta\varphi)} - f\,\delta\lambda_i(\delta\Delta\varphi) \end{bmatrix} \tag{3.10}$$

Considering that the boresight angles and the impact of boresight roll angle variation on the scale factor – $\boldsymbol{\delta\lambda_i(\delta\Delta\varphi)}$ – are small values, the second order incremental terms in Equation 3.10 (in bold) can be ignored. Thus, Equation 3.10 could be reduced to the form in Equation 3.11.

$$\delta r_I^m(\delta\Delta\varphi) = \lambda_i \begin{bmatrix} \mp f\delta\Delta\varphi \\ 0 \\ -x_i\delta\Delta\varphi \end{bmatrix} + \begin{bmatrix} \pm x_i\delta\lambda_i(\delta\Delta\varphi) \\ 0 \\ -f\delta\lambda_i(\delta\Delta\varphi) \end{bmatrix} \tag{3.11}$$

To simplify Equation 3.11 further, the impact of variation in the boresight roll on the scale factor $\left(\delta\lambda_i(\delta\Delta\varphi)\right)$ can be derived with the help of Figure 3.6. For a vertical scanner, given an image point $\boldsymbol{i}$ and corresponding object point $\boldsymbol{I}$, the scale factor can be defined as $\lambda_i = \frac{PI}{Pi} = \frac{H}{f}$, where $\boldsymbol{P}$ denotes the perspective center of the push-broom scanner. As can be seen in Figure 3.6, the scale factor as a function of the boresight roll angle ($\Delta\varphi$) is represented by Equation 3.12, where the term $\cos(\theta - \Delta\varphi)$ can be expanded according to Equation 3.13 while assuming small boresight roll angle $\Delta\varphi$.

$$\lambda_i'(\Delta\varphi) = \frac{PI'}{Pi'} = \frac{PI'}{\left(f^2 + x_i^2\right)^{0.5}}, \text{ where } PI' = H/\cos(\theta - \Delta\varphi) \tag{3.12}$$

$$\cos(\theta - \Delta\varphi) = \cos\theta\cos\Delta\varphi + \sin\theta\sin\Delta\varphi \cong \cos\theta + \Delta\varphi\sin\theta \tag{3.13}$$

As per Figure 3.6, the distance PI' can be derived according to Equations 3.14 and 3.15.

$$PI' = \frac{H}{\cos\theta + \sin\theta\,\Delta\varphi} = \frac{H/\cos\theta}{1 + \tan\theta\,\Delta\varphi} \cong \frac{H}{\cos\theta}(1 - \tan\theta\,\Delta\varphi) \tag{3.14}$$

$$PI' = \frac{H}{f/(f^2 + x_i{}^2)^{0.5}}\left(1 - \frac{x_i}{f}\Delta\varphi\right) \tag{3.15}$$

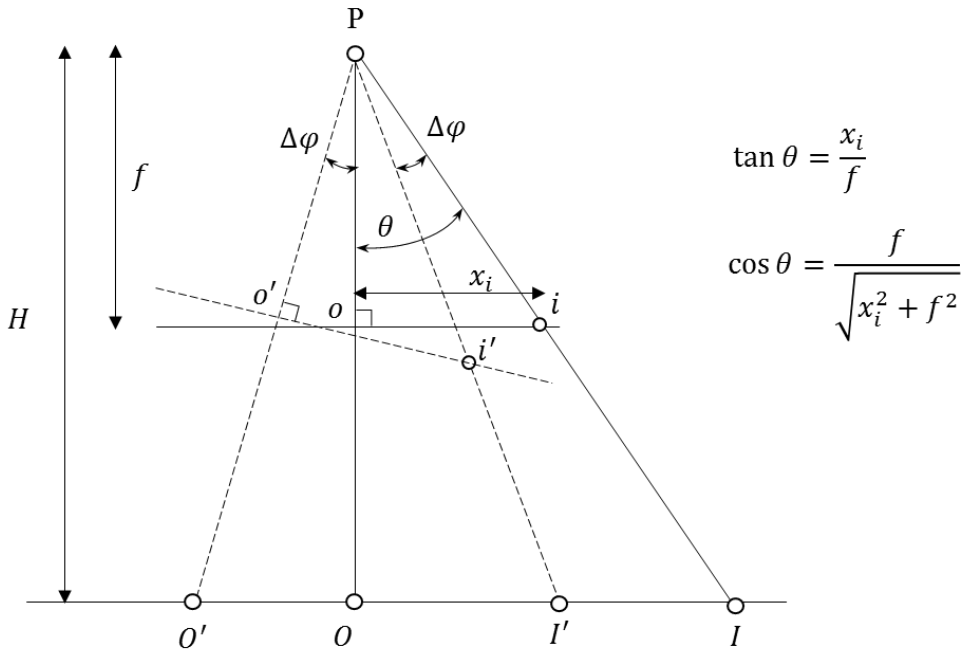

Figure 3.6: Incremental change in the scale factor due to the variation in the boresight roll angle

Since $Pi' = Pi = (f^2 + x_i^2)^{0.5}$, the scale factor as a function of the boresight roll angle ($\Delta\varphi$) can be represented by Equation 3.16.

$$\lambda_i'(\Delta\varphi) = \frac{H}{f}\left(1 - \frac{x_i}{f}\Delta\varphi\right) = \frac{H}{f} - \frac{H}{f^2}x_i\Delta\varphi \tag{3.16}$$

As a result, the change in the scale factor due to incremental change in the boresight roll angle can be derived, Equation 3.17.

$$\delta\lambda_i(\delta\Delta\varphi) = -\frac{H}{f^2}x_i\,\delta\Delta\varphi \tag{3.17}$$

Finally, the impact of incremental change in the boresight roll angle ($\delta\Delta\varphi$) on the ground coordinates can be presented by Equations 3.18 and 3.19, where $\boldsymbol{X_I'}$ is the lateral distance between the object point and flight trajectory.

$$\delta r_I^m(\delta\Delta\varphi) = \lambda_i \begin{bmatrix} \mp f\delta\Delta\varphi \\ 0 \\ -x_i\delta\Delta\varphi \end{bmatrix} + \begin{bmatrix} \pm x_i(-\frac{H}{f^2})x_i\,\delta\Delta\varphi \\ 0 \\ -f(-\frac{H}{f^2})x_i\,\delta\Delta\varphi \end{bmatrix} \tag{3.18}$$

$$\delta r_I^m(\delta\Delta\varphi) = \begin{bmatrix} \mp H\delta\Delta\varphi \mp \frac{X_I'^2}{H}\delta\Delta\varphi \\ 0 \\ -X_I'\delta\Delta\varphi + X_I'\delta\Delta\varphi \end{bmatrix} = \begin{bmatrix} \mp\left(H + \frac{X_I'^2}{H}\right)\delta\Delta\varphi \\ 0 \\ 0 \end{bmatrix} \tag{3.19}$$

According to the above bias impact analysis, the total impact of boresight angle variations on the ground coordinates is given by Equation 3.20.

$$\delta r_I^m(\delta\Delta\omega, \delta\Delta\varphi, \delta\Delta\kappa) = \begin{bmatrix} \mp\left(H + \frac{X_I'^2}{H}\right)\delta\Delta\varphi \\ \pm H\delta\Delta\omega \pm X_I'\delta\Delta\kappa \\ 0 \end{bmatrix} \tag{3.20}$$

Based on that equation, one can state the following:

1) A bias in the boresight pitch angle ($\delta\Delta\omega$) will impact the coordinates along the flight direction. The impact of this bias on the ground coordinates depends on the platform's flying height and flying direction.
2) A bias in the boresight roll angle ($\delta\Delta\varphi$) will impact the coordinates across the flight direction. The impact of this bias on the ground coordinates depends on flying height, flight direction, and lateral distance between the point in question and the flight trajectory.
3) A bias in the boresight heading ($\delta\Delta\kappa$) will impact the coordinates along the flight direction. The impact of such variation on the ground coordinates is flying direction independent (as the impact of the ± signs will be nullified by the sign of the lateral distance $-\boldsymbol{X_I'}-$ when flying in different directions). The impact increases as the lateral distance between the control/tie points in question and trajectory increases. For control/tie points that are directly below the flight trajectory (i.e., $\boldsymbol{x_i}\ and\ \boldsymbol{X_I'} \cong 0$), then $\delta r_I^m(\delta\Delta\kappa) \cong 0$, which implies that

the boresight heading angle cannot be estimated if the control/tie points are aligned along the center of the swath covered by the push-broom scan lines.

3.4 Optimal/Minimal Configuration of Flight Lines and Control/Tie Points

Based on the above findings, the optimal/minimal configuration of flight lines and control/tie points for the estimation of the boresight angles can be summarized as follows:

1) For a GCP-based approach, a single flight line and two GCPs – with one aligned along the center of the covered swath and the other point aligned along the edge of the covered swath – are needed (Figure 3.7-a). The GCP aligned along the swath center will allow for the estimation of the boresight pitch and roll angles ($\Delta\omega$ and $\Delta\varphi$) by minimizing the discrepancies along and across the flight line (the impact of the boresight heading angle at that point would be quite minimal). The point at the edge of the swath will allow for the estimation of the boresight heading angle ($\Delta\kappa$).
2) For a tie point-based approach, three flight lines and a single tie point would be needed. Two of the flight lines should be in opposite directions and have 100% overlap. The third flight line should be parallel to one of the first two with an overlap of roughly 50%. The tie point could be located along the center of the scan covered by the third flight line (Figure 3.7-b). Enforcing the coplanarity of the light rays associated with the identified tie point in the opposite scans with 100% overlap would allow for the estimation of the boresight pitch and roll angles ($\Delta\omega$ and $\Delta\varphi$) – one should note that since the impact of a bias in the boresight heading is flying direction independent, $\delta\Delta\kappa$ will not impact the coplanarity of the conjugate light rays for those flight lines. On the other hand, enforcing the coplanarity of the light rays associated with the identified tie point in the parallel flight lines with 50% overlap will ensure the estimation of the boresight heading angle ($\Delta\kappa$).

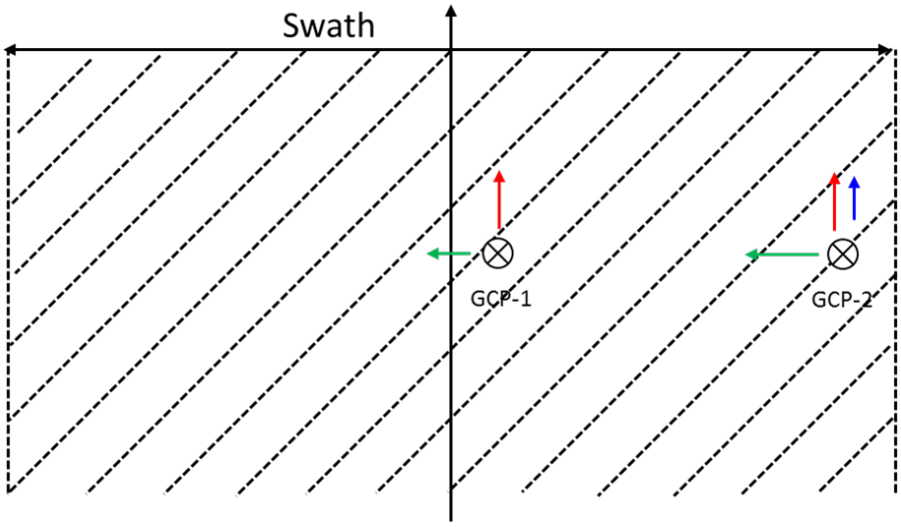

(a)

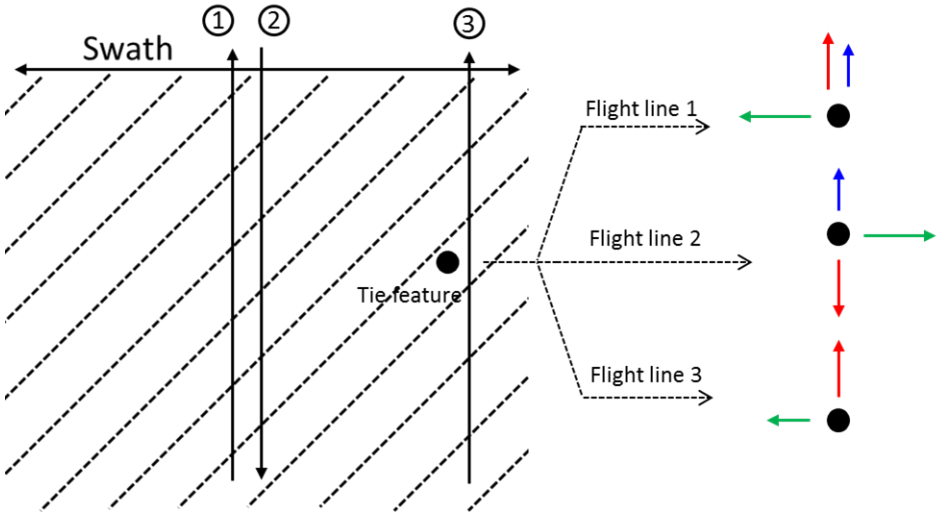

(b)

Figure 3.7: Optimal/minimal flight configuration for (a) GCP-based approach, and (b) tie-point-based approach, where the red, green, and blue arrows represent the impact of a bias in the boresight pitch, roll, and heading angles ($\delta\Delta\omega$, $\delta\Delta\varphi$, and $\delta\Delta\kappa$), respectively. The dashed areas represent the swath covered by the central flight line(s).

In practice, it is recommended to use more GCPs/tie point features to derive an estimate of the evaluated boresight angles while minimizing the impact of random errors in the system

measurements as well as improve the ability to detect gross errors in such measurements (i.e., improving the reliability of the adjustment procedure).

3.5 Summary

In this chapter, to ensure reliable/practical estimation of the boresight angles, a bias impact analysis is conducted based on the collinearity equations. Such bias impact is established by evaluating the changes in the ground coordinates of derived object points as a result of biases in the boresight angles. Then, the derived impact is adopted to set the optimal flight and control/tie point configuration. The optimal/minimal configuration of flight lines is presented for GCP-based approach and tie-point based approach separately.

4. BORESIGHT CALIBRATION STRATEGIES

4.1 Overview

This chapter starts by introducing an approximate calibration procedure utilizing tie points in overlapping scenes. This procedure is based on the previously discussed bias impact analysis. Then, two rigorous approaches, which use GCPs and tie points, are introduced. As mentioned earlier, the approximate and rigorous approaches are based on enforcing the collinearity and coplanarity of light rays connecting the perspective centers of the imaging scanner, object point, and the respective image points.

4.2 Approximate Boresight Calibration using Tie Points

First, we propose an approximate boresight calibration strategy, which is based on the use of tie points and some of the stated assumptions for the bias impact analysis. More specifically, the boresight angles are estimated by enforcing the intersection of the light rays connecting the perspective centers of the scan lines encompassing the corresponding image points of the tie point and the respective conjugate image points (i.e., enforcing the coplanarity constraint). To relax the requirement for having almost parallel IMU and scanner coordinate systems (i.e., we are always dealing with small boresight angles), one can introduce a virtual scanner coordinate system – denoted by $\boldsymbol{c'}$ – that is almost parallel to the original scanner frame – denoted by $\boldsymbol{c}$. The boresight matrix relating the virtual scanner, $\boldsymbol{c'}$, to the IMU body frame ($\boldsymbol{R_{c'}^{b}}$) can be set by the user to represent the nominal relationship between the scanner and IMU body frame coordinate systems. Therefore, the boresight rotation matrix $\boldsymbol{R_{c}^{b}}$ can be decomposed into two rotation matrices as $R_{c}^{b} = R_{c'}^{b} R_{c}^{c'}$, where $R_{c}^{c'}$ is an unknown incremental boresight rotation matrix that is defined by

incremental boresight pitch, roll, and heading angles $(\Delta\omega, \Delta\varphi, \Delta\kappa)$. Thus, the collinearity equations can be represented by the form in Equation 4.1.

$$r_I^m = r_b^m(t) + R_b^m(t)\, r_c^b + \lambda_i\, R_{c'}^m(t)\, R_c^{c'} r_i^c, \text{ where } R_{c'}^m(t) = R_b^m(t)\, R_{c'}^b \tag{4.1}$$

Another assumption that could be relaxed is the one related to having a push-broom scanner, which is flown along the *South-to-North* and *North-to-South* directions. In cases where the flight lines do not adhere to this assumption, one can manipulate the trajectory position and orientation $\boldsymbol{r_b^m(t)}$ and $\boldsymbol{R_b^m(t)}$ information so they are defined relative to a mapping frame that is parallel to the flight directions.

After such manipulation, the rotation matrix $\boldsymbol{R_{c'}^m(t)}$ will take the form in Equation 4.1. At this stage, it is worth mentioning that the decomposition of the boresight matrix also eliminates the need for having the IMU body frame axes aligned along the starboard, forward, and up directions since we will be working with $\boldsymbol{R_{c'}^m(t)}$ rather than $\boldsymbol{R_b^m(t)}$.

Following the above assumption relaxation procedure, we are only left with the strict requirements for having almost vertical scanner over a relatively flat terrain. For an identified tie point in multiple flight lines, the derived ground coordinates using the nominal values for the boresight angles (i.e., assuming $\Delta\omega, \Delta\varphi, \Delta\kappa$ to be zeros) can be derived according to Equation 4.2.

$$\begin{aligned} r_I^m(estimated) &= r_I^m(true) + \delta r_I^m(\delta\Delta\omega, \delta\Delta\varphi, \delta\Delta\kappa) \\ &= r_I^m(true) + \begin{bmatrix} \mp\left(H + \dfrac{{X'_I}^2}{H}\right)\delta\Delta\varphi \\ \pm H\delta\Delta\omega \pm X'_I\delta\Delta\kappa \\ 0 \end{bmatrix} \end{aligned} \tag{4.2}$$

So, for a tie point in overlapping scenes, the difference between the estimated ground coordinates from the respective flight lines – denoted as $\boldsymbol{a}$ and $\boldsymbol{b}$ – could be represented by Equation 4.3, where $\boldsymbol{X'_a}$ and $\boldsymbol{X'_b}$ represent the lateral distance between the corresponding object point and

the $\boldsymbol{a}$ and $\boldsymbol{b}$ flight trajectories. If a tie point is captured in $\boldsymbol{n}$ image strips, one of them is regarded as a reference and the remaining $(n-1)$ occurrences are paired with it to produce $(n-1)$ sets of equations of the form in Equation 4.3.

$$r_I^m(a, estimated) - r_I^m(b, estimated) = \begin{bmatrix} \mp\left(H + \frac{X_a'^2}{H}\right)\delta\Delta\varphi \\ \pm H\delta\Delta\omega \pm X_a'\delta\Delta\kappa \\ 0 \end{bmatrix} - \begin{bmatrix} \mp\left(H + \frac{X_b'^2}{H}\right)\delta\Delta\varphi \\ \pm H\delta\Delta\omega \pm X_b'\delta\Delta\kappa \\ 0 \end{bmatrix} \quad (4.3)$$

Using a flight and tie point configuration that meets the stated optimal/minimal flight configuration for tie-point-based approach (Figure 3.7-b), we will have 4 equations (of the form in Equation 4.3) from the formulated pairs – the Z-difference between the projected points will not be used as they are not related to biases in the incremental boresight angles – in three unknowns. Thus, these equations can be used in Least Squares Adjustment (LSA) to solve for biases in the boresight angles $\delta\Delta\omega, \delta\Delta\varphi$, and $\delta\Delta\kappa$. Since this approach estimates biases in the boresight angles, the boresight angles defining the matrix $R_c^{c\prime}$will be $-\delta\Delta\omega, -\delta\Delta\varphi, -\delta\Delta\kappa$. Finally, the boresight rotation matrix ($\boldsymbol{R_c^b}$) is derived by multiplying the nominal boresight rotation matrix ($\boldsymbol{R_{c'}^b}$) and the incremental boresight matrix ($\boldsymbol{R_c^{c'}}$), which is defined by ($-\delta\Delta\omega, -\delta\Delta\varphi$, and $-\delta\Delta\kappa$).

4.3 Rigorous Boresight Calibration using GCPs

In this section, a rigorous boresight calibration procedure that uses identified GCPs in the acquired push-broom hyperspectral scenes is presented. The proposed procedure is based on a reformulated collinearity equation model where the image coordinates are represented as a function of the GNSS/INS position and orientation, ground coordinates of the GCP, lever arm components, and the boresight angles as represented by Equation 4.4.

$$r_i^c = {}^1/_{\lambda_i} R_b^c \{ R_m^b(t) [r_I^m - r_b^m(t)] - r_c^b \} \tag{4.4}$$

To avoid running into the gimbal lock problem (i.e., the secondary rotation angle of R_c^b is 90°), the boresight matrix $\boldsymbol{R_c^b}$ is decomposed into the product of two rotation matrices $\boldsymbol{R_{c'}^b}$ and $\boldsymbol{R_c^{c'}}$ – where $\boldsymbol{c'}$ represents a virtual scanner. Similar to the approximate approach, the virtual scanner coordinate system – $\boldsymbol{c'}$ – is set up to be almost parallel to the original scanner coordinate system – $\boldsymbol{c}$. In such a case, $\boldsymbol{R_{c'}^b}$ will be a known rotation matrix that depends on the alignment of the scanner relative to the IMU body frame and $\boldsymbol{R_c^{c'}}$ will be defined by the unknown incremental rotation in Equation 3.3. Therefore, Equation 4.4 could be reformulated to the form in Equation 4.5, which can be simplified as in Equation 4.6.

$$r_i^c = {}^1/_{\lambda_i} R_{c'}^c R_b^{c'} \{ R_m^b(t) [r_I^m - r_b^m(t)] - r_c^b \} \tag{4.5}$$

$$r_i^c = {}^1/_{\lambda_i} \begin{bmatrix} 1 & -\Delta\kappa & \Delta\varphi \\ \Delta\kappa & 1 & -\Delta\omega \\ -\Delta\varphi & \Delta\omega & 1 \end{bmatrix} \begin{bmatrix} N_X \\ N_Y \\ D \end{bmatrix} \tag{4.6}$$

where $\begin{bmatrix} N_X \\ N_Y \\ D \end{bmatrix} = R_b^{c'} \{ R_m^b(t) [r_I^m - r_b^m(t)] - r_c^b \}$

One should note that $[N_X \quad N_Y \quad D]^T$ in Equation 4.6 is fully defined by the ground coordinates of the GCPs, internal characteristics of the scanner, GNSS/INS position and orientation information, lever arm components, and nominal boresight matrix ($\boldsymbol{R_{c'}^b}$). To eliminate the unknown scale factor $\boldsymbol{\lambda_i}$ from Equation 4.6, the first and second rows can be divided by the third one to produce Equations 4.7 and 4.8, which are non-linear in the unknown boresight angles ($\Delta\omega, \Delta\varphi, \Delta\kappa$).

$$\frac{x_i}{-f} = \frac{N_X - N_Y\Delta\kappa + D\Delta\varphi}{-N_X\Delta\varphi + N_Y\Delta\omega + D} \tag{4.1}$$

$$\frac{y_i}{-f} = \frac{N_X\Delta\kappa + N_Y - D\Delta\omega}{-N_X\Delta\varphi + N_Y\Delta\omega + D} \tag{4.2}$$

Adopting a similar approach to the Direct Linear Transformation (DLT) [24], this non-linear relationship can be re-expressed in a linear form as per Equations 4.9 and 4.10. For each image point corresponding to a given GCP, two equations in three unknowns can be derived.

$$x_i(-N_X\Delta\varphi + N_Y\Delta\omega + D) = -f(N_X - N_Y\Delta\kappa + D\Delta\varphi) \quad (4.9)$$

$$y_i(-N_X\Delta\varphi + N_Y\Delta\omega + D) = -f(N_X\Delta\kappa + N_Y - D\Delta\omega) \quad (4.10)$$

Having a minimal configuration similar to the optimal/minimal flight configuration for GCP-based approach presented in Figure 3.7-a, four equations can be formulated and used to solve for the incremental boresight angles defining $\boldsymbol{R_c^{c'}}$, which could be used to derive the boresight matrix $\boldsymbol{R_c^b}$ as the product of $\boldsymbol{R_{c'}^b}$ and $\boldsymbol{R_c^{c'}}$.

Besides the boresight angles, other parameters, such as focal length, can be included in the GCP-based calibration procedure. In this case, the mathematical model becomes non-linear in the involved unknowns. Meanwhile, minimal/optimal flight configuration has to be modified to ensure the reliable estimation.

4.4 Rigorous Boresight Calibration using Tie Points

Rather than using GCPs, this approach is based on using identified tie points in the push-broom scanner scenes to estimate the boresight angles. As stated earlier, the boresight angles are estimated by enforcing the coplanarity constraint relating conjugate points in overlapping push-broom hyperspectral scenes. Similar to the previous approach, situations leading to a gimbal lock could be mitigated by introducing a virtual scanner – $\boldsymbol{c'}$ – that is almost parallel to the original scanner and using a known nominal boresight rotation matrix ($\boldsymbol{R_{c'}^b}$) relating the IMU body frame and the virtual scanner coordinate systems. Therefore, the unknown boresight angles would be the incremental angles $(\Delta\omega, \Delta\varphi, \Delta\kappa)$ defining $\boldsymbol{R_c^{c'}}$. The used mathematical model is the one represented

by Equations 4.7 and 4.8 where both the incremental boresight angles ($\Delta\omega, \Delta\varphi, \Delta\kappa$) and the ground coordinates of the tie points $\boldsymbol{r_I^m}$ are unknowns.

Since one is dealing with a non-linear model in the involved unknowns, an iterative LSA procedure should be used starting from approximate values of the unknowns. For the incremental boresight angles, $\Delta\omega, \Delta\varphi,$ and $\Delta\kappa$ can be assumed to be zeros. This assumption is quite valid since rotational relationship to be solved is between the original and virtual scanner coordinate systems. The approximate values for the ground coordinates of the tie points can be derived using Equation 4.1 while assuming vertical imagery over relatively flat terrain (thus the scale factor can be approximated by the ratio between the flying height above ground and the scanner principal distance – i.e., $\lambda_i = \frac{H}{f}$).

Using the optimal/minimal flight and tie point configuration suggested in Figure 3.7-b, one will have six equations in six unknowns; namely the incremental boresight angles and the ground coordinates of the tie point in question. One should note that using more flight lines and/or tie points is highly recommended. Similar to the previous calibration strategies, the boresight rotation matrix ($\boldsymbol{R_c^b}$) is derived by multiplying the nominal boresight rotation matrix ($\boldsymbol{R_{c'}^b}$) and the incremental boresight matrix ($\boldsymbol{R_c^{c'}}$).

4.5 Summary

Three different calibration strategies are introduced in this chapter. The first approach is an approximate calibration strategy using tie points. Boresight angles are estimated based on bias impact analysis. The other two approaches are rigorous with one using GCPs while the other relying on tie points. The GCP-based rigorous approach aims at minimizing the differences

between the projected object points onto the image space and the observed image points for the used GCPs. The tie-point-based rigorous approach aims to enforce the coplanarity principle.

5. EXPERIMENTAL RESULTS

5.1 Data Acquisition System Description

In this study, the hyperspectral data has been acquired using a Headwall Nano-Hyperspec push-broom scanner (shown in Figure 5.1) and Headwall Hyperspec SWIR push-broom scanner (shown in Figure 5.2). Headwall Nano-Hyperspec sensor covers 272 spectral bands ranging between 400 nm and 1000 nm with a band width of 2.2 nm [25]. Each scan line contains 640 pixels with a pixel pitch of 7.4 μm. The focal length of the used Nano-Hyperspec push-broom scanner is 12.7 mm, which corresponds to roughly 3.5 cm GSD when flying at 60 m above ground.

The Headwall Hyperspec SWIR push-broom scanner covers 267 spectral bands ranging between 900 nm and 2500 nm with a band width of 9.6 nm [26]. Each scan line contains 384 pixels with a pixel pitch of 24 μm. The focal length is 25 mm, and the corresponding GSD is roughly 3.8 cm at 40 m flying height.

Figure 5.1: Headwall Nano-Hyperspec push-broom scanner

Figure 5.2: Headwall Hyperspec SWIR push-broom scanner

A Trimble APX-15 UAV (V2) (Figure 5.3), which is designed for small UAVs, was integrated with the hyperspectral scanners to directly provide the position and orientation of the scanner. The APX unit, which has been fitted in a housing to accommodate a wiring harness, is attached to the hyperspectral scanners via threaded fasteners, as shown in Figure 5.4. The POSPac MMS Differential GNSS Inertial post-processing software from Applanix was used for post processing of the raw GNSS/IMU data. After post processing of the integrated GNSS/IMU data, the accuracy of position and orientation estimation is expected to be around 2-5 cm for position, 0.025° for pitch and roll angles, and 0.080° for the heading angle [27].

Figure 5.3: Trimble APX-15 UAV (V2)

Figure 5.4: Trimble APX-15 UAV (V2) attached to the Nano-Hyperspec push-broom scanner

For the conducted experimental results, two different unmanned aerial platforms from DJI were used to acquire the hyperspectral data. The first platform was the Spreading Wings S1000+ (Figure 5.5) and the second is the Matrice 600 Pro (M600) shown in Figure 5.6.

Figure 5.5: DJI S1000+ with Nano-Hyperspec and APX-15 UAV (V2)

Figure 5.6: DJI Matrice 600 with DJI Ronin MX 3-axis brushless gimbal

These two platforms are designed for professional aerial photography and industrial applications. Unlike the M600, the S1000+ did not use a standard DJI A2 flight controller. Instead, an open-source Pixhawk 2 flight controller was installed. For integrating the Nano-Hyperspec with the airframes, two approaches were used. For the S1000+, the Nano-Hyperspec was rigidly mounted directly to the airframe. However, a DJI Ronin MX 3-axis brushless gimbal stabilizer (Figure 5.7) was used on the larger M600 airframe. By using the gimbal, the sensor maintains a nadir view regardless of airframe orientation. This capability produces clearer scenes for identifying the required control/tie points for the different boresight calibration strategies. For Hyperspec SWIR, the scanner was rigidly mounted on M600 without using the gimbal.

Figure 5.8 shows the coordinate systems definition for the Nano-Hyperspec and IMU systems mounted on UAVs. In Figure 5.9, one can see that the nominal boresight matrix relating the IMU and virtual scanner coordinate systems ($R_b^{c'}$) can be defined with -90 degrees primary rotation around Z axis, 0 degree secondary rotation around Y axis, and 90 degrees tertiary rotation around

X axis ($R_Z(-90)\ R_Y(0)\ R_X(90)$). It is also evident that the IMU body frame is not setup with its xyz-axes aligned along the starboard, forward, and up directions, respectively.

Figure 5.7: DJI Ronin MX 3-axis brushless gimbal stabilizer that maintains the scanner in nadir view

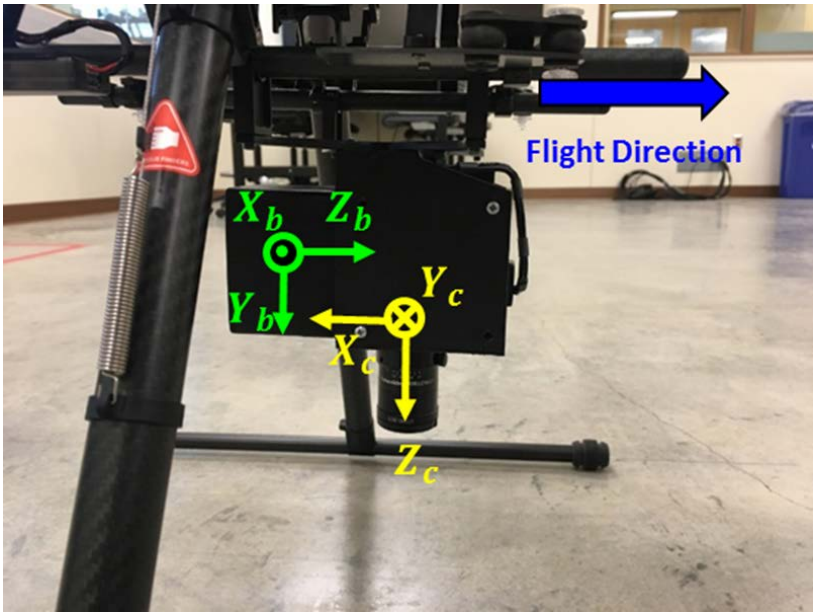

Figure 5.8: Definitions of coordinate systems for the Nano-Hyperspec scanner and APX-15 UAV (V2) mounted on S1000+

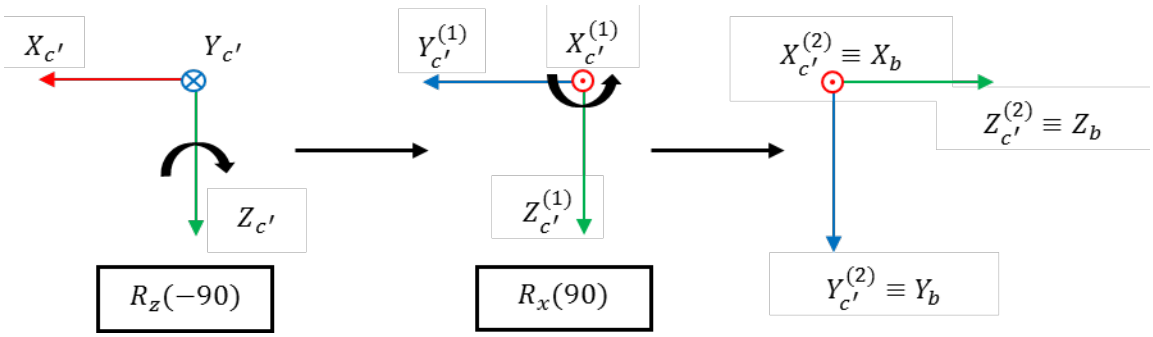

Figure 5.9: The nominal boresight matrix relating the IMU and virtual scanner coordinate systems ($R_b^{c'}$)

Figure 5.10 depicts the coordinate systems definition for the Hyperspec SWIR push-broom scanner and IMU body frame. The nominal boresight matrix relating the IMU and virtual scanner coordinate systems ($R_b^{c'}$) can be defined with 90 degrees primary rotation around Z axis, 0 degree secondary rotation around Y axis, and 90 degrees tertiary rotation around X axis ($R_Z(90)\, R_Y(0)\, R_X(90)$).

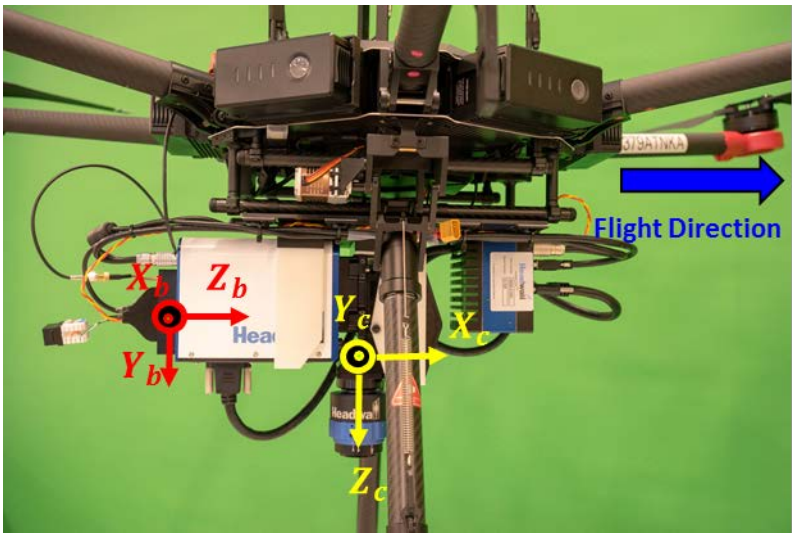

Figure 5.10: Definitions of coordinate systems for the Hyperspec SWIR scanner and APX-15 UAV (V2) mounted on M600

5.2 Data Description

For this study, ten datasets using Headwall Nano-Hyperspec and Headwall Hyperspec SWIR push-broom scanner were acquired during the summer of 2017. The experimental location is an agricultural test field within the Agronomy Center for Research and Education (ACRE) at Purdue University (Figure 5.11).

Figure 5.11: Test field used with five checkerboard targets

Five checkerboard targets, which were used as either tie points or GCPs, were deployed in the field. The ground coordinates of all the checkerboard targets were surveyed by a Topcon GR-5 GNSS receiver with an accuracy of 2-3 cm. The checkerboard targets are identified in the original hyperspectral scenes and the image point coordinates are measured using Envi 4.5.4 software. Table 5.1 describes the collection dates, type of hyperspectral push-broom scanner, platform used, and altitude/ground speed for each flight. For datasets captured using Nano-Hyperspec on July 30th and August 1st, a gimbal stabilizer is adopted.

Table 5.1 Flight Specifications of the Collected Datasets

Collection Date	Push-broom Scanner	UAV	Gimbal Stabilizer	Altitude	Speed
July 12th, 15th, 18th, and 25th	Nano	S1000+	No	60 m	5 m/s
July 30th and August 1st	Nano	M600	Yes		
August 2nd, 8th, 14th, 23rd	SWIR	M600	No	40 m	8 m/s

Figure 5.12 shows a top view of the flight trajectory for the Nano August 1st dataset and SWIR August 13th with three highlighted segments. Portion A in the figure includes the UAV trajectory while performing required GNSS/IMU dynamic alignment before and after the flight mission. Portion B depicts the used flight lines for boresight calibration over the checkerboard targets. In Portion C, the Nano-Hyperspec and Hyperspec SWIR collected data, which is used to qualitatively evaluate the performance of the boresight calibration through the generated ortho-rectified mosaics over a sorghum field.

The calibration flight lines for Nano-Hyperspec are oriented in the *East-West* direction (contrary to the *South-North* assumption). Six flight lines are used: a) two overlapping flight lines in opposite directions over the targets; b) two overlapping flight lines in opposite directions 7 meters north of the targets; c) two overlapping flight lines in opposite directions 7 meters south of the targets. For the Hyperspec SWIR dataset, only 4 flight lines oriented in the *East-West* direction are used: a) two overlapping flight lines in opposite directions over the targets; b) one *East-to-West* flight line 7 meters north of the targets; c) one *West-to-East* flight line 7 meters south of the targets.

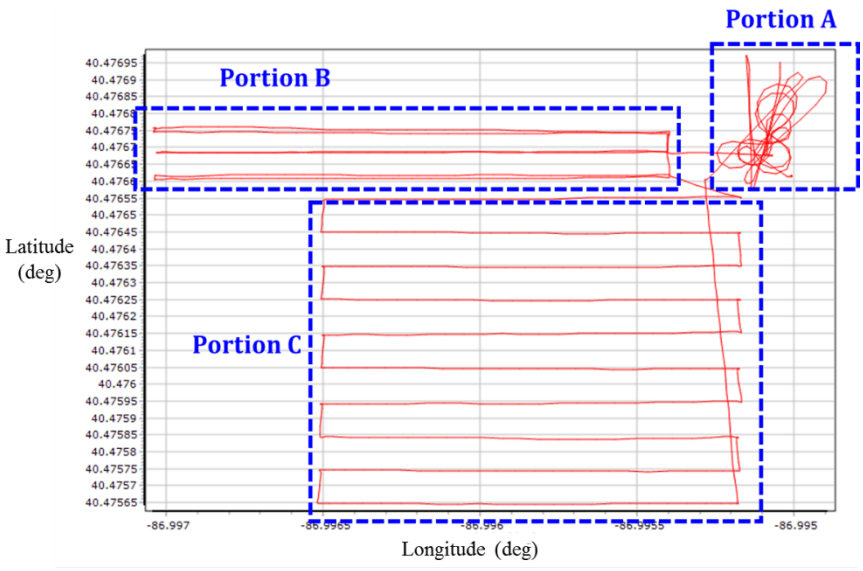

(a)

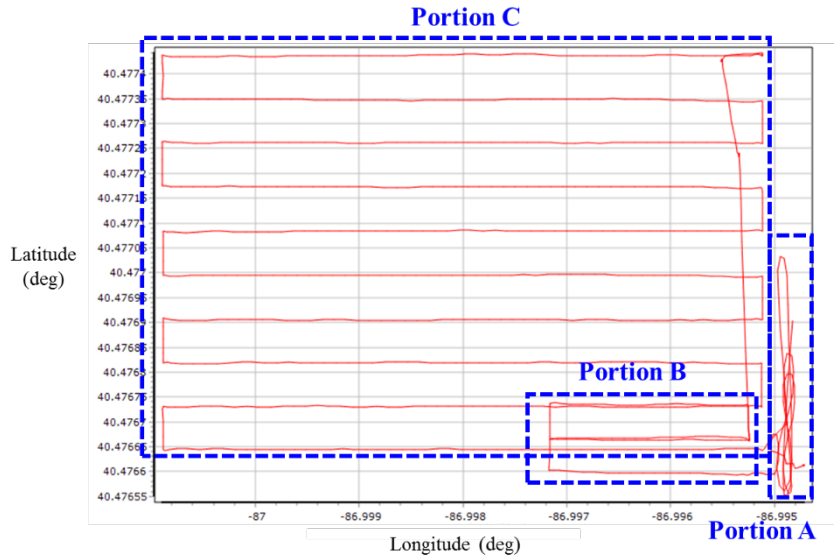

(b)

Figure 5.12: Top view of the flight trajectory: Portion A – dynamic alignment of the GNSS/IMU unit, Portion B – boresight calibration flight lines, and Portion C – flight lines used to capture hyperspectral data for the generation of ortho-rectified mosaics, (a) Nano August 1st dataset, (b) SWIR August 14th dataset

5.3 Results and Analysis

First, the proposed optimal/minimal flight and control/tie point configuration is verified through boresight calibration using proposed configuration. Then, general boresight calibration results for several datasets are presented. To evaluate the accuracy of proposed approaches, qualitative and quantitative evaluations are conducted by visually checking the generated ortho-rectified mosaics and derived ground coordinates of the targets, respectively.

5.3.1 Calibration Results for Minimal Flight and Control/Tie Point Configuration

The main objective of this portion of the experimental results is verifying the feasibility of the proposed optimal/minimal flight and control/tie point configuration in estimating the mounting parameters. To do so, we ran the GCP-based and tie-point-based rigorous calibration procedures using the configurations in Figure 5.13, which are subset of the Nano August 1st dataset.

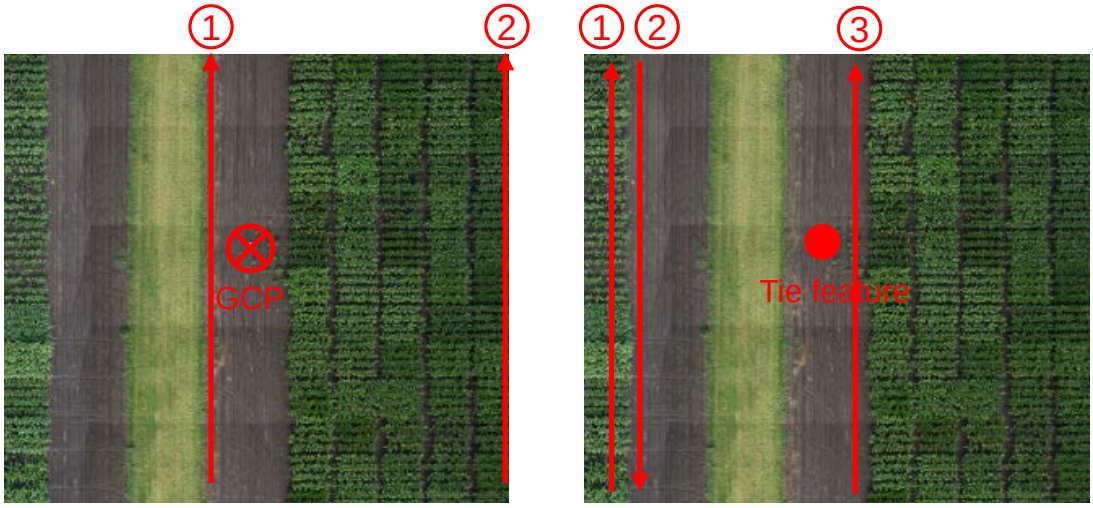

(a) (b)

Figure 5.13: Optimal/minimal flight and control/tie point configuration for (a) the GCP-based and (b) tie-point-based rigorous calibration strategies.

As can be seen from the dataset description section, we only have collinear control targets. Therefore, instead of using a single flight line and two control points for the GCP-based rigorous approach, we used a single GCP and two flight lines with some lateral distance in between. Tables

5.2 and 5.3 report the estimated boresight angles together with the associated correlation matrix for both approaches. For the GCP-based rigorous calibration strategy, we have four equations in three unknowns (the incremental boresight angles). Therefore, we can derive an estimate for the standard deviation of the estimated parameters. For the tie-point-based rigorous calibration, on the other hand, we have six equations in six unknowns (the incremental boresight angles and the ground coordinates of the tie point). Therefore, for this calibration approach, the minimal configuration cannot provide an estimate for the standard deviation of the derived boresight angles (the a-posteriori variance component cannot be evaluated due to the zero redundancy).

Table 5.2 Nominal and Estimated Boresight Angles From the GCP-based and Tie-point-based Rigorous Calibration Strategies for the Optimal/Minimal Flight and Control/Tie Point Configuration in Figure 5.13.

Approach	ω (°)	φ (°)	κ (°)
Nominal value	90	0	-90
Rigorous–GCP	90.253 ±0.063	0.524 ±0.069	-90.389 ±0.869
Rigorous–Tie Points	90.260	0.469	-91.179

Table 5.3 Correlation Matrix for the Estimated Boresight Angles Using (a) GCP-based and (b) Tie-point-based Rigorous Calibration Strategies for the Optimal/Minimal Flight and Control/Tie Point Configuration in Figure 5.13.

(a)

	$\Delta\omega$	$\Delta\varphi$	$\Delta\kappa$
$\Delta\omega$	1.000	-0.025	0.064
$\Delta\varphi$	-0.025	1.000	-0.393
$\Delta\kappa$	0.064	-0.393	1.000

(b)

	$\Delta\omega$	$\Delta\varphi$	$\Delta\kappa$
$\Delta\omega$	1.000	-0.240	0.082
$\Delta\varphi$	-0.240	1.000	-0.094
$\Delta\kappa$	0.082	-0.094	1.000

In Table 5.2, one can see that the standard deviation of the boresight heading angle for the GCP-based rigorous calibration is significantly higher when compared to those for the boresight pitch and roll angles. This is mainly attributed to the relatively small lateral distance (7 m) between the GCP and the flight trajectory – this lateral distance is crucial for the estimation of the boresight heading angle. Based on the reported results (especially the correlation matrices, where one can note low correlation among the estimated boresight angles), one can see that the minimal configuration is capable of deriving an estimate of the boresight angles. The impact of adding more flight lines and control/tie points and the improvements in the ortho-rectified mosaics will be shown in the next section.

5.3.2 General Calibration Results

The initial nominal values for the boresight angles and the estimated ones of Nano-Hyperspec scanner system along with their standard deviations from the three proposed calibration strategies, while using the six calibration flights and five targets as GCPs/tie points, are presented in Table 5.4, where one can see that the boresight calibration results from the GCP-based rigorous and tie-point-based rigorous approaches are almost identical. This similarity should be expected since these approaches adopt the rigorous collinearity equations without incurring any assumptions. For the approximate strategy, on the other hand, the reported standard deviations for the estimated boresight angles are larger than those for the rigorous approaches.

The correlation matrices for the estimated boresight angles from the different strategies/dates are presented in Tables 5.5-5.10. Such correlation matrices indicate that none of the parameters are highly correlated, which verifies the validity of the suggested optimal calibration configuration.

Table 5.11 presented the boresight calibration results for Hyperspec SWIR datasets where the standard deviations of estimated boresight angles are compatible with the results of Nano-

Hyperspec. Correlation matrices from these datasets are listed in Tables 5.12-5.15 showing low correlation between boresight angles.

Table 5.4 Nominal and Estimated Boresight Angles from the Approximate, GCP-based Rigorous, and Tie-point-based Rigorous Calibration Strategies for Nano-Hyperspec datasets

Collection Date	Approach	ω (°)	φ (°)	κ (°)
	Nominal value	90	0	-90
July 12th, 2017	Approximate–Tie Points	90.208 ±0.024	0.637 ±0.024	-92.093 ±0.425
	Rigorous–GCP	90.284 ±0.018	0.545 ±0.018	-91.169 ±0.206
	Rigorous–Tie Points	90.244 ±0.017	0.549 ±0.024	-91.329 ±0.256
July 15th, 2017	Approximate–Tie Points	90.214 ±0.025	0.488 ±0.021	-91.146 ±0.487
	Rigorous–GCP	90.262 ±0.013	0.527 ±0.013	-90.212 ±0.118
	Rigorous–Tie Points	90.259 ±0.012	0.527 ±0.014	-90.215 ±0.110
July 18th, 2017	Approximate–Tie Points	90.262 ±0.027	0.533 ±0.026	-88.570 ±0.429
	Rigorous–GCP	90.209 ±0.026	0.498 ±0.027	-90.466 ±0.225
	Rigorous–Tie Points	90.206 ±0.022	0.502 ±0.025	-90.641 ±0.181
July 25th, 2017	Approximate–Tie Points	90.273 ±0.037	0.512 ±0.023	-89.939 ±0.456
	Rigorous–GCP	90.251 ±0.019	0.511 ±0.019	-90.386 ±0.194
	Rigorous–Tie Points	90.232 ±0.019	0.508 ±0.022	-90.337 ±0.193
July 30th, 2017	Approximate–Tie Points	90.268 ±0.014	0.495 ±0.012	-89.972 ±0.255
	Rigorous–GCP	90.270 ±0.012	0.512 ±0.012	-90.429 ±0.114
	Rigorous–Tie Points	90.277 ±0.010	0.509 ±0.010	-90.366 ±0.105
August 1st, 2017	Approximate–Tie Points	90.236 ±0.013	0.489 ±0.013	-90.820 ±0.285
	Rigorous–GCP	90.271 ±0.011	0.492 ±0.011	-90.510 ±0.107
	Rigorous–Tie Points	90.259 ±0.013	0.493 ±0.014	-90.485 ±0.115

Table 5.5 Correlation Matrix of Boresight Angles Estimates for Nano-Hyperspec July 12th Dataset: (a) Approximate, (b) GCP-based Rigorous, and (c) Tie-point-based Rigorous Calibration Strategies.

(a)

	$\Delta\omega$	$\Delta\varphi$	$\Delta\kappa$
$\Delta\omega$	1.000	0.000	-0.121
$\Delta\varphi$	0.000	1.000	0.000
$\Delta\kappa$	-0.121	0.000	1.000

(b)

	$\Delta\omega$	$\Delta\varphi$	$\Delta\kappa$
$\Delta\omega$	1.000	0.004	0.056
$\Delta\varphi$	0.004	1.000	0.072
$\Delta\kappa$	0.056	0.072	1.000

(c)

	$\Delta\omega$	$\Delta\varphi$	$\Delta\kappa$
$\Delta\omega$	1.000	-0.050	0.094
$\Delta\varphi$	-0.050	1.000	0.001
$\Delta\kappa$	0.094	0.001	1.000

Table 5.6 Correlation Matrix of Boresight Angles Estimates for Nano-Hyperspec July 15th Dataset: (a) Approximate, (b) GCP-based Rigorous, and (c) Tie-point-based Rigorous Calibration Strategies.

(a)

	$\Delta\omega$	$\Delta\varphi$	$\Delta\kappa$
$\Delta\omega$	1.000	0.000	0.472
$\Delta\varphi$	0.000	1.000	0.000
$\Delta\kappa$	0.472	0.000	1.000

(b)

	$\Delta\omega$	$\Delta\varphi$	$\Delta\kappa$
$\Delta\omega$	1.000	-0.002	0.040
$\Delta\varphi$	-0.002	1.000	-0.037
$\Delta\kappa$	0.040	-0.037	1.000

(c)

	$\Delta\omega$	$\Delta\varphi$	$\Delta\kappa$
$\Delta\omega$	1.000	0.004	0.042
$\Delta\varphi$	0.004	1.000	-0.087
$\Delta\kappa$	0.042	-0.087	1.000

Table 5.7 Correlation Matrix of Boresight Angles Estimates for Nano-Hyperspec July 18th Dataset: (a) Approximate, (b) GCP-based Rigorous, and (c) Tie-point-based Rigorous Calibration Strategies.

(a)

	$\Delta\omega$	$\Delta\varphi$	$\Delta\kappa$
$\Delta\omega$	1.000	0.000	0.240
$\Delta\varphi$	0.000	1.000	0.000
$\Delta\kappa$	0.240	0.000	1.000

(b)

	$\Delta\omega$	$\Delta\varphi$	$\Delta\kappa$
$\Delta\omega$	1.000	-0.002	0.031
$\Delta\varphi$	-0.002	1.000	-0.058
$\Delta\kappa$	0.031	-0.058	1.000

(c)

	$\Delta\omega$	$\Delta\varphi$	$\Delta\kappa$
$\Delta\omega$	1.000	-0.014	0.063
$\Delta\varphi$	-0.014	1.000	-0.078
$\Delta\kappa$	0.063	-0.078	1.000

Table 5.8 Correlation Matrix of Boresight Angles Estimates for Nano-Hyperspec July 25th Dataset: (a) Approximate, (b) GCP-based Rigorous, and (c) Tie-point-based Rigorous Calibration Strategies.

(a)

	$\Delta\omega$	$\Delta\varphi$	$\Delta\kappa$
$\Delta\omega$	1.000	0.000	0.589
$\Delta\varphi$	0.000	1.000	0.000
$\Delta\kappa$	0.589	0.000	1.000

(b)

	$\Delta\omega$	$\Delta\varphi$	$\Delta\kappa$
$\Delta\omega$	1.000	0.005	0.043
$\Delta\varphi$	0.005	1.000	0.126
$\Delta\kappa$	0.043	0.126	1.000

(c)

	$\Delta\omega$	$\Delta\varphi$	$\Delta\kappa$
$\Delta\omega$	1.000	-0.049	0.047
$\Delta\varphi$	-0.049	1.000	0.141
$\Delta\kappa$	0.047	-0.141	1.000

Table 5.9 Correlation Matrix of Boresight Angles Estimates for Nano-Hyperspec July 30th Dataset: (a) Approximate, (b) GCP-based Rigorous, and (c) Tie-point-based Rigorous Calibration Strategies.

(a)

	$\Delta\omega$	$\Delta\varphi$	$\Delta\kappa$
$\Delta\omega$	1.000	0.000	0.485
$\Delta\varphi$	0.000	1.000	0.000
$\Delta\kappa$	0.485	0.000	1.000

(b)

	$\Delta\omega$	$\Delta\varphi$	$\Delta\kappa$
$\Delta\omega$	1.000	0.005	0.045
$\Delta\varphi$	0.005	1.000	-0.006
$\Delta\kappa$	0.045	-0.006	1.000

(c)

	$\Delta\omega$	$\Delta\varphi$	$\Delta\kappa$
$\Delta\omega$	1.000	-0.008	0.046
$\Delta\varphi$	-0.008	1.000	0.010
$\Delta\kappa$	0.046	0.010	1.000

Table 5.10 Correlation Matrix of Boresight Angles Estimates for Nano-Hyperspec August 1st Dataset: (a) Approximate, (b) GCP-based Rigorous, and (c) Tie-point-based Rigorous Calibration Strategies.

(a)

	$\Delta\omega$	$\Delta\varphi$	$\Delta\kappa$
$\Delta\omega$	1.000	0.000	0.235
$\Delta\varphi$	0.000	1.000	0.000
$\Delta\kappa$	0.235	0.000	1.000

(b)

	$\Delta\omega$	$\Delta\varphi$	$\Delta\kappa$
$\Delta\omega$	1.000	0.003	0.045
$\Delta\varphi$	0.003	1.000	0.065
$\Delta\kappa$	0.045	0.065	1.000

(c)

	$\Delta\omega$	$\Delta\varphi$	$\Delta\kappa$
$\Delta\omega$	1.000	0.010	0.041
$\Delta\varphi$	0.010	1.000	0.049
$\Delta\kappa$	0.041	0.049	1.000

Table 5.11 Nominal and Estimated Boresight Angles from the Approximate, GCP-based Rigorous, and Tie-point-based Rigorous Calibration Strategies for Hyperspec SWIR datasets

Collection Date	Approach	ω (°)	φ (°)	κ (°)
	Nominal value	90	0	90
August 2nd, 2017	Approximate–Tie Points	90.006 ±0.023	0.167 ±0.021	90.052 ±0.664
	Rigorous–GCP	90.007 ±0.030	0.220 ±0.031	89.890 ±0.267
	Rigorous–Tie Points	89.897 ±0.018	0.226 ±0.023	89.926 ±0.148
August 8th, 2017	Approximate–Tie Points	89.896 ±0.041	0.309 ±0.030	90.597 ±0.668
	Rigorous–GCP	89.993 ±0.027	0.386 ±0.032	88.900 ±0.293
	Rigorous–Tie Points	89.893 ±0.028	0.311 ±0.039	88.813 ±0.282
August 14th, 2017	Approximate–Tie Points	90.044 ±0.025	0.150 ±0.021	90.635 ±0.672
	Rigorous–GCP	90.014 ±0.022	0.241 ±0.022	89.852 ±0.188
	Rigorous–Tie Points	89.923 ±0.012	0.245 ±0.014	89.873 ±0.104
August 23rd, 2017	Approximate–Tie Points	90.052 ±0.027	0.175 ±0.026	90.594 ±0.466
	Rigorous–GCP	89.995 ±0.021	0.279 ±0.022	89.659 ±0.204
	Rigorous–Tie Points	89.933 ±0.015	0.266 ±0.018	89.686 ±0.150

Table 5.12 Correlation Matrix of Boresight Angles Estimates for Hyperspec SWIR August 2nd Dataset: (a) Approximate, (b) GCP-based Rigorous, and (c) Tie-point-based Rigorous Calibration Strategies.

(a)

	$\Delta\omega$	$\Delta\varphi$	$\Delta\kappa$
$\Delta\omega$	1.000	0.000	0.316
$\Delta\varphi$	0.000	1.000	0.000
$\Delta\kappa$	0.316	0.000	1.000

(b)

	$\Delta\omega$	$\Delta\varphi$	$\Delta\kappa$
$\Delta\omega$	1.000	0.000	-0.001
$\Delta\varphi$	0.000	1.000	0.126
$\Delta\kappa$	-0.001	0.126	1.000

(c)

	$\Delta\omega$	$\Delta\varphi$	$\Delta\kappa$
$\Delta\omega$	1.000	0.095	0.010
$\Delta\varphi$	0.095	1.000	0.115
$\Delta\kappa$	0.010	0.115	1.000

Table 5.13 Correlation Matrix of Boresight Angles Estimates for Hyperspec SWIR August 8th Dataset: (a) Approximate, (b) GCP-based Rigorous, and (c) Tie-point-based Rigorous Calibration Strategies.

(a)

	$\Delta\omega$	$\Delta\varphi$	$\Delta\kappa$
$\Delta\omega$	1.000	0.000	0.664
$\Delta\varphi$	0.000	1.000	0.000
$\Delta\kappa$	0.664	0.000	1.000

(b)

	$\Delta\omega$	$\Delta\varphi$	$\Delta\kappa$
$\Delta\omega$	1.000	-0.007	0.013
$\Delta\varphi$	-0.007	1.000	-0.502
$\Delta\kappa$	0.013	-0.502	1.000

(c)

	$\Delta\omega$	$\Delta\varphi$	$\Delta\kappa$
$\Delta\omega$	1.000	-0.337	0.032
$\Delta\varphi$	-0.337	1.000	-0.469
$\Delta\kappa$	0.032	-0.469	1.000

Table 5.14 Correlation Matrix of Boresight Angles Estimates for Hyperspec SWIR August 14th Dataset: (a) Approximate, (b) GCP-based Rigorous, and (c) Tie-point-based Rigorous Calibration Strategies.

(a)

	$\Delta\omega$	$\Delta\varphi$	$\Delta\kappa$
$\Delta\omega$	1.000	0.000	0.535
$\Delta\varphi$	0.000	1.000	0.000
$\Delta\kappa$	0.535	0.000	1.000

(b)

	$\Delta\omega$	$\Delta\varphi$	$\Delta\kappa$
$\Delta\omega$	1.000	0.000	-0.002
$\Delta\varphi$	0.000	1.000	0.043
$\Delta\kappa$	-0.002	0.043	1.000

(c)

	$\Delta\omega$	$\Delta\varphi$	$\Delta\kappa$
$\Delta\omega$	1.000	0.034	-0.036
$\Delta\varphi$	0.034	1.000	0.048
$\Delta\kappa$	-0.036	0.048	1.000

Table 5.15 Correlation Matrix of Boresight Angles Estimates for Hyperspec SWIR August 23rd Dataset: (a) Approximate, (b) GCP-based Rigorous, and (c) Tie-point-based Rigorous Calibration Strategies.

(a)

	$\Delta\omega$	$\Delta\varphi$	$\Delta\kappa$
$\Delta\omega$	1.000	0.000	-0.095
$\Delta\varphi$	0.000	1.000	0.000
$\Delta\kappa$	-0.095	0.000	1.000

(b)

	$\Delta\omega$	$\Delta\varphi$	$\Delta\kappa$
$\Delta\omega$	1.000	0.000	0.000
$\Delta\varphi$	0.000	1.000	0.071
$\Delta\kappa$	0.000	0.070	1.000

(c)

	$\Delta\omega$	$\Delta\varphi$	$\Delta\kappa$
$\Delta\omega$	1.000	0.069	-0.069
$\Delta\varphi$	0.069	1.000	0.115
$\Delta\kappa$	-0.069	0.115	1.000

5.3.3 Qualitative Analysis

The accuracy of the estimated boresight angles is qualitatively checked by visually inspecting the ortho-rectified mosaics of Portion C in Figure 5.12 for the different datasets/dates generated using the nominal and estimated boresight angles from the different calibration strategies. The ortho-rectified mosaics are generated by the Hyperspec III Software [28] from Headwall. Due to the visual similarity of the post-calibration ortho-rectified mosaics from the different approaches, we only show the results from the tie-point-based rigorous calibration for Nano-Hyperspec system. Figure 5.14 shows the ortho-rectified mosaics for the July 15th dataset. Visible misalignments in parts A and B while using the nominal boresight angles are quite obvious. Zoomed-in areas at those locations are also included in Figure 5.14 for closer inspection. These misalignments have been eliminated in the post-calibrated ortho-rectified mosaics. The ortho-rectified mosaics for the Nano July 25th and Nano August 1st are presented in Figures 5.15 and 5.16, respectively. Since the differences between nominal boresight angles and estimated boresight angles after calibration are minor for the Hyperspec SWIR system, the ortho-rectified mosaics using either nominal boresight angles or estimated boresight angles are of good quality without obvious misalignments.

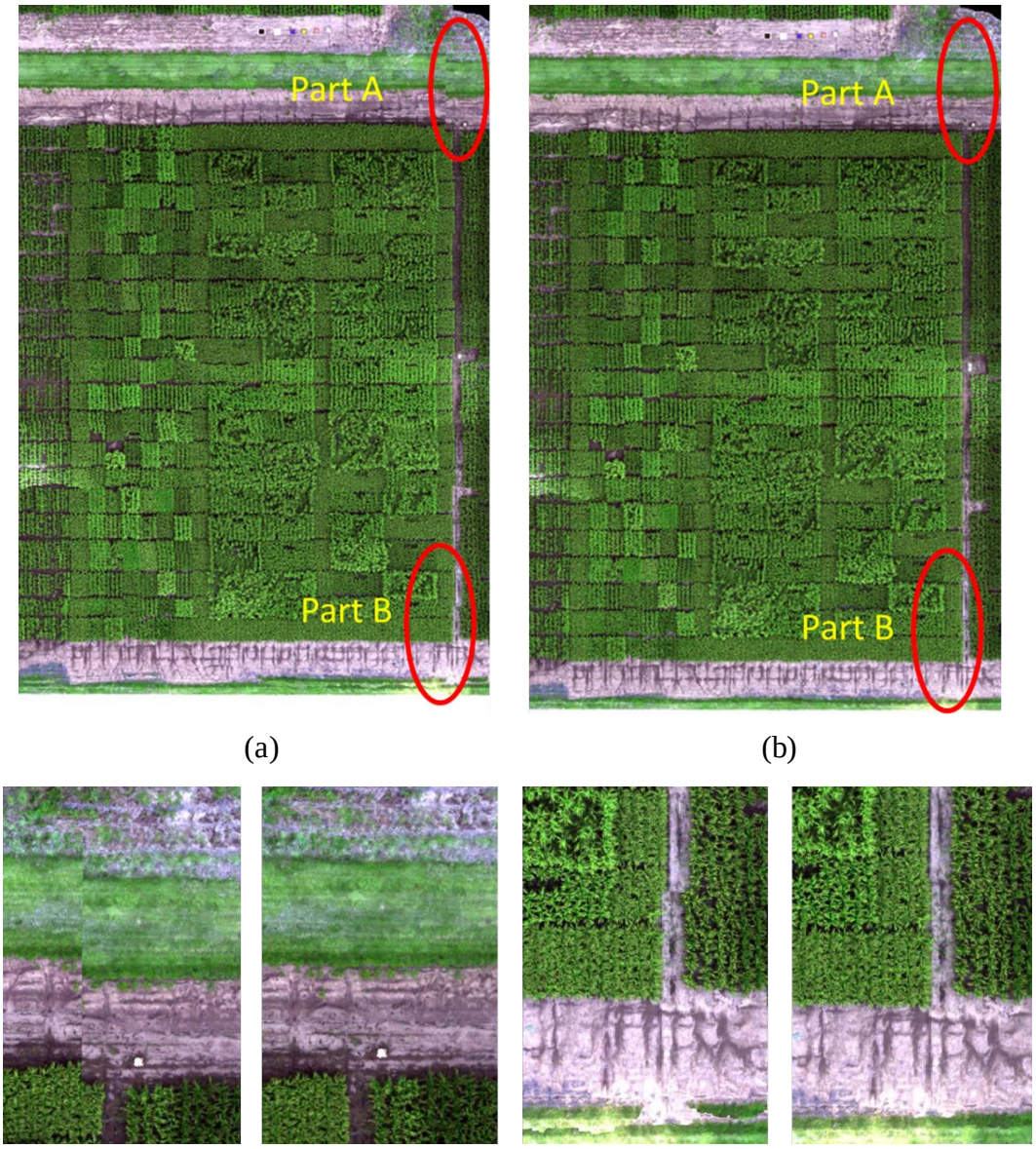

Figure 5.14: Generated ortho-rectified mosaics for the Nano-Hyperspec July 15th dataset: (a) using nominal boresight angles, (b) using the tie-point-based rigorous calibration estimates of the boresight angles, (c) and (d) zoomed-in areas for parts A and B, respectively before (left) and after (right) the calibration process.

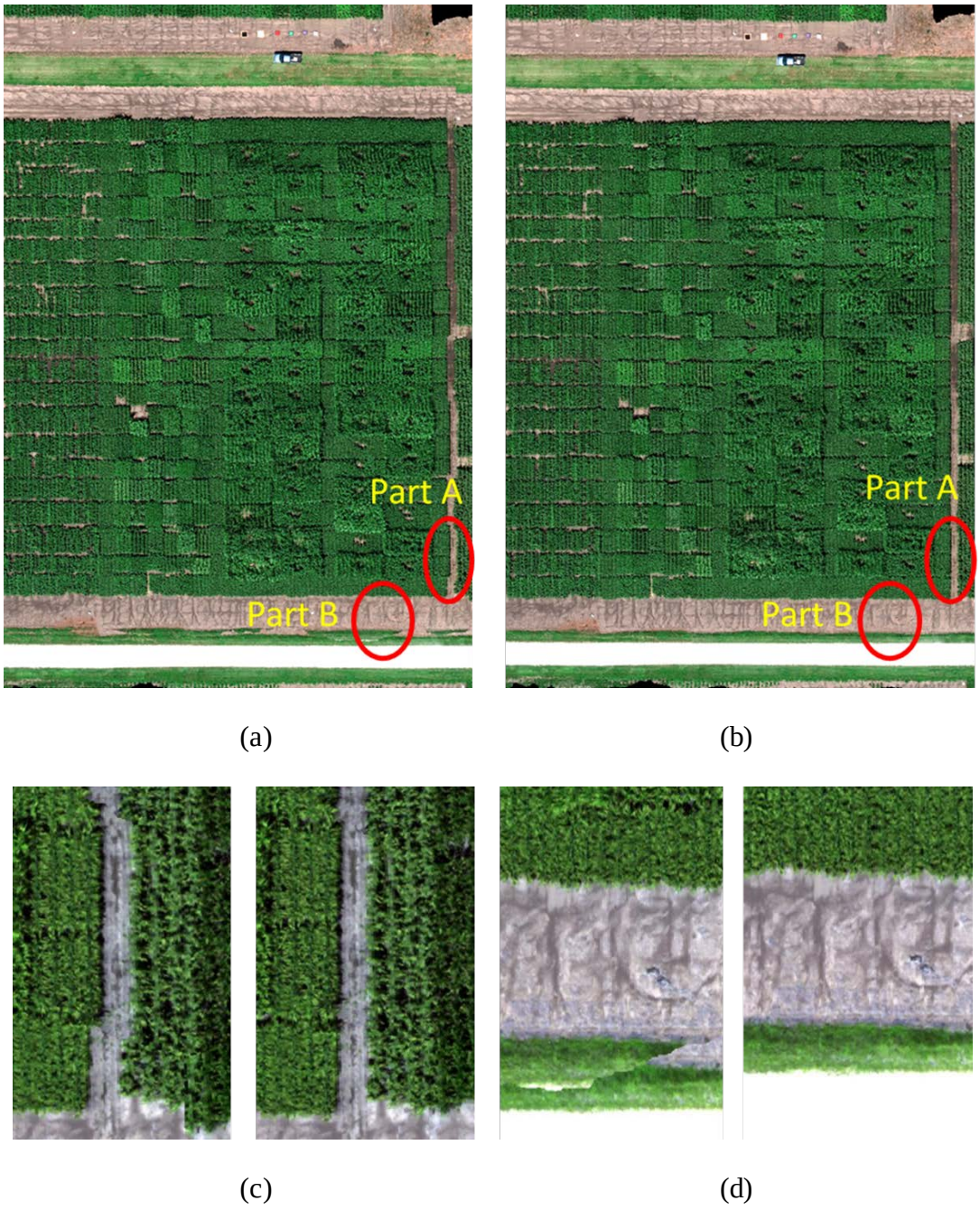

Figure 5.15: Generated ortho-rectified mosaics for the Nano-Hyperspec July 25th dataset: (a) using nominal boresight angles, (b) using the tie-point-based rigorous calibration estimates of the boresight angles, (c) and (d) zoomed-in areas for parts A and B, respectively before (left) and after (right) the calibration process.

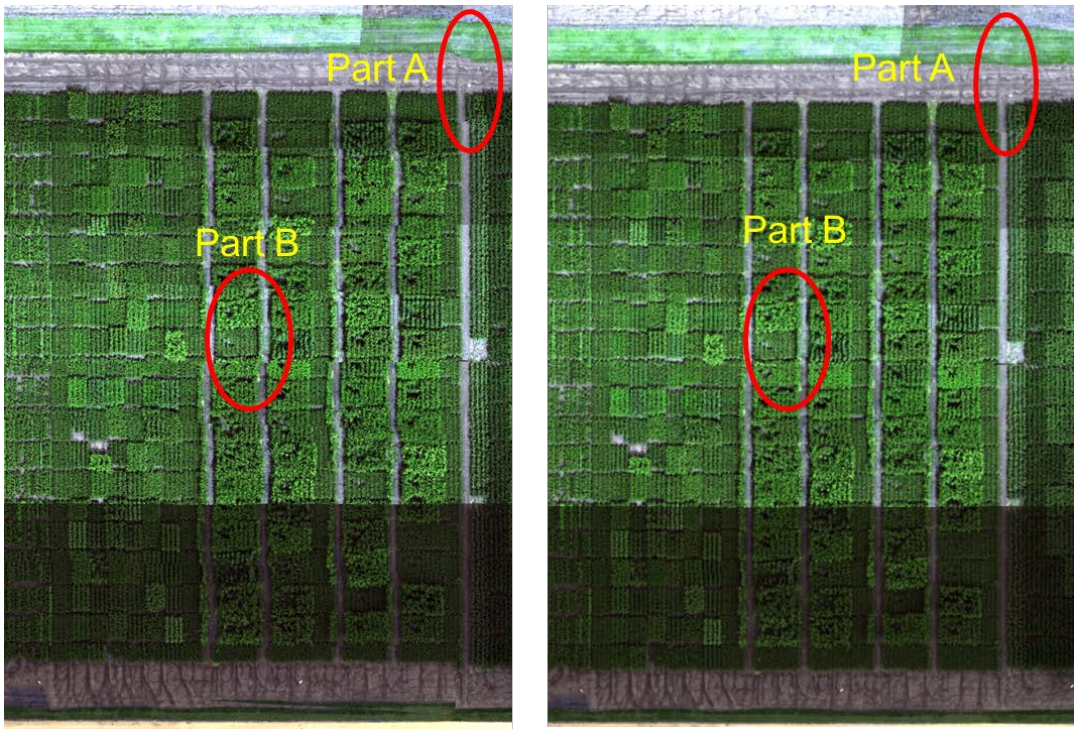

(a) (b)

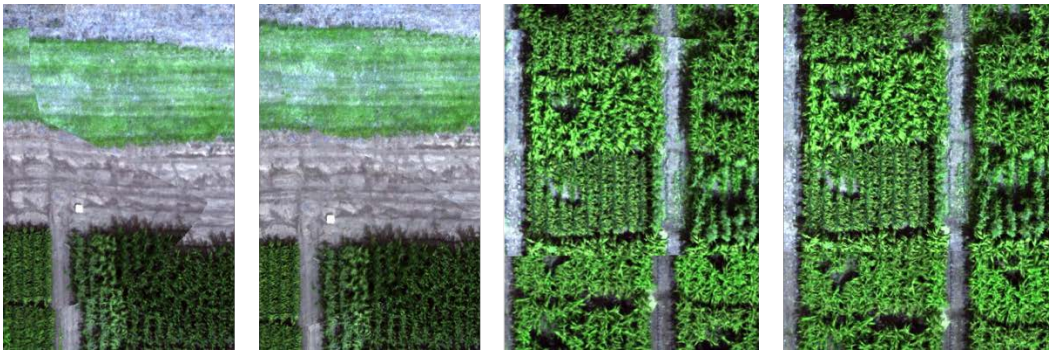

(c) (d)

Figure 5.16: Generated ortho-rectified mosaics for the Nano-Hyperspec August 1st dataset: (a) using nominal boresight angles, (b) using the tie-point-based rigorous calibration estimates of the boresight angles, (c) and (d) zoomed-in areas for parts A and B, respectively before (left) and after (right) the calibration process.

5.3.4 Quantitative Analysis

In terms of quantitative evaluation of the boresight calibration accuracy, derived ground coordinates from the different calibration strategies are compared with the surveyed coordinates of the checkerboard targets. For the approximate and GCP-based rigorous calibration strategies, the ground coordinates are derived by projecting the image points onto an assumed flat terrain. For the before calibration, the nominal values of the boresight angles were used. For the tie-point-based boresight calibration strategy, the XYZ coordinates of the tie points are derived from the calibration procedure together with the boresight angles. The evaluated ground coordinates are then compared with the surveyed coordinates by the Topcon GR-5 GNSS receiver. Tables 5.16 and 5.17 report the RMSE of the differences along the XYZ directions for Nano-Hyperspec datasets and Hyperspec SWIR datasets, respectively.

Assuming that well-identified targets/features are available, the RMSE value that can be tolerated is at the level of the GSD of the used sensor. It can be seen from Table 5.16 that all the calibration strategies had a major impact on improving the planimetric accuracy of derived ground coordinates with the tie-point-based calibration producing the most accurate results for the Nano-Hyperspec datasets. Since the GCP derivation for the approximate and GCP-based rigorous calibration procedures projects the image points onto a flat terrain, the vertical differences are quite similar to those derived using the nominal values. Therefore, one could conclude that vertical differences are mainly attributed to the flat terrain assumption and not due to the quality of the available boresight angles since the derived Z coordinate is based on nominal average flying height. This hypothesis has been confirmed by the conducted bias impact analysis, where we have shown that biases in the boresight angles will not lead to biases in the vertical ground coordinates. For the tie-point-based calibration strategy, the RMSE in the vertical direction is much better – however, it is significantly worse than the planimetric RMSE.

Table 5.16 RMSE of the Differences between the Derived and Surveyed Ground Coordinates Before and After the Different Boresight Calibration Strategies for Nano-Hyperspec Datasets

Collection Date	Approach	RMSE of X coordinate residuals (m)	RMSE of Y coordinate residuals (m)	RMSE of Z coordinate residuals (m)
July 12th, 2017	Before Boresight Calibration	0.305	0.648	1.096
	Approximate–Tie Points	0.125	0.135	1.096
	Rigorous–GCP	0.118	0.129	1.096
	Rigorous–Tie Points	0.062	0.055	0.594
July 15th, 2017	Before Boresight Calibration	0.273	0.538	0.870
	Approximate–Tie Points	0.150	0.106	0.870
	Rigorous–GCP	0.106	0.099	0.870
	Rigorous–Tie Points	0.054	0.035	0.352
July 18th, 2017	Before Boresight Calibration	0.277	0.490	0.770
	Approximate–Tie Points	0.287	0.115	0.770
	Rigorous–GCP	0.165	0.105	0.770
	Rigorous–Tie Points	0.116	0.045	0.288
July 25th, 2017	Before Boresight Calibration	0.311	0.505	0.739
	Approximate–Tie Points	0.145	0.098	0.739
	Rigorous–GCP	0.145	0.096	0.739
	Rigorous–Tie Points	0.057	0.029	0.387
July 30th, 2017	Before Boresight Calibration	0.295	0.560	0.419
	Approximate–Tie Points	0.080	0.069	0.419
	Rigorous–GCP	0.063	0.066	0.419
	Rigorous–Tie Points	0.050	0.040	0.173
August 1st, 2017	Before Boresight Calibration	0.262	0.540	0.456
	Approximate–Tie Points	0.085	0.042	0.456
	Rigorous–GCP	0.080	0.042	0.456
	Rigorous–Tie Points	0.033	0.012	0.223

Table 5.17 RMSE of the Differences between the Derived and Surveyed Ground Coordinates Before and After the Different Boresight Calibration Strategies for Hyperspec SWIR Datasets

Collection Date	Approach	RMSE of X coordinate residuals (m)	RMSE of Y coordinate residuals (m)	RMSE of Z coordinate residuals (m)
August 2nd, 2017	Before Boresight Calibration	0.069	0.171	0.459
	Approximate–Tie Points	0.072	0.100	0.459
	Rigorous–GCP	0.070	0.100	0.459
	Rigorous–Tie Points	0.040	0.032	0.971
August 8th, 2017	Before Boresight Calibration	0.138	0.239	0.505
	Approximate–Tie Points	0.149	0.050	0.505
	Rigorous–GCP	0.085	0.062	0.505
	Rigorous–Tie Points	0.042	0.022	0.848
August 14th, 2017	Before Boresight Calibration	0.075	0.178	0.545
	Approximate–Tie Points	0.119	0.127	0.545
	Rigorous–GCP	0.071	0.135	0.545
	Rigorous–Tie Points	0.025	0.028	0.825
August 23rd, 2017	Before Boresight Calibration	0.066	0.217	0.254
	Approximate–Tie Points	0.099	0.129	0.254
	Rigorous–GCP	0.060	0.113	0.254
	Rigorous–Tie Points	0.029	0.036	0.535

The accuracy of derived X and Y coordinates for Hyperspec SWIR datasets, as listed in Table 5.17, are quite identical to Nano-Hyperspec. However, the RMSE of Z coordinates residuals are higher for tie-point-based calibration strategy. Considering that boresight angles have no impact

on the vertical ground coordinates, the worse Z-accuracy is probably caused by inaccurate focal length provided by specification. To prove this hypothesis, the focal length f is estimated in GCP-based approach for four SWIR datasets. The estimation of focal length f is around 24.5 mm instead of 25 mm in the specification.

Then, tie-point-based boresight calibration are conducted for four SWIR datasets again using new estimated focal length. Table 5.18 shows the RMSE of Z coordinates residuals derived from tie-point-based approach using nominal and estimated focal length. The improvement of Z-accuracy proves that inaccurate focal length leads to the large RMSE of Z residuals for Hyperspec SWIR datasets.

At this stage, the relatively worse vertical accuracy as represented by the RMSE is hypothesized to be caused by the intersection geometry for conjugate light rays. To verify or reject this hypothesis, average standard deviations of the estimated ground coordinates for tie points from the tie-point-based rigorous adjustment procedure are evaluated (the mean standard deviations for Nano-Hyperspec and Hyperspec SWIR datasets are reported in Tables 5.19 and 5.20).

The compatibility of the RMSE and mean standard deviations for the XYZ directions as derived from the tie-point-based rigorous calibration proves that the above hypothesis (i.e., the quality of the vertical coordinates depends on the intersection geometry rather than the quality of the boresight angles) is correct. Moreover, it also shows the absence of systematic errors/biases. A final observation that can be drawn from the presented results is the impact of having a gimbal on the data acquisition platform. As it can be seen in Tables 5.17 and 5.19, the Nano July 30th and August 1st datasets, which were captured by the M600 using a gimbal, produced the best results (almost at the same level as the GSD of the sensor). This performance is attributed to the clearer scenes, which contributed to better identification of the image space features.

Table 5.18 RMSE of the Differences between the Derived and Surveyed Ground Coordinates from the Tie-point-based Boresight Calibration Strategy Using Nominal/Estimated Focal Length for Hyperspec SWIR Datasets

Collection Date	Focal Length	RMSE of X coordinate residuals (m)	RMSE of Y coordinate residuals (m)	RMSE of Z coordinate residuals (m)
August 2nd, 2017	25 mm (Nominal)	0.040	0.032	0.971
	24.5 mm (Estimated)	0.033	0.032	0.234
August 8th, 2017	25 mm (Nominal)	0.042	0.022	0.848
	24.5 mm (Estimated)	0.044	0.032	0.166
August 14th, 2017	25 mm (Nominal)	0.025	0.028	0.825
	24.5 mm (Estimated)	0.028	0.019	0.100
August 23rd, 2017	25 mm (Nominal)	0.029	0.036	0.535
	24.5 mm (Estimated)	0.027	0.051	0.289

Table 5.19 Mean Standard Deviations for the Estimated Ground Coordinates of Tie Points from the Tie-point-based Rigorous Calibration Strategy for Nano-Hyperspec Datasets

Collection Date	Mean STD of estimated X coordinates (m)	Mean STD of estimated Y coordinates (m)	Mean STD of estimated Z coordinates (m)
July 12th, 2017	±0.049	±0.050	±0.447
July 15th , 2017	±0.029	±0.036	±0.291
July 18th , 2017	±0.048	±0.049	±0.367
July 25th, 2017	±0.049	±0.045	±0.430
July 30th, 2017	±0.026	±0.027	±0.325
August 1st, 2017	±0.031	±0.030	±0.268

Table 5.20 Mean Standard Deviations for the Estimated Ground Coordinates of Tie Points from the Tie-point-based Rigorous Calibration Strategy for Hyperspec SWIR Datasets

Collection Date	Mean STD of estimated X coordinates (m)	Mean STD of estimated Y coordinates (m)	Mean STD of estimated Z coordinates (m)
August 2nd, 2017	±0.029	±0.028	± 0.201
August 8th , 2017	±0.044	±0.042	±0.347
August 14th , 2017	±0.022	±0.022	±0.162
August 23rd, 2017	±0.027	±0.029	±0.206

6. CONCLUSIONS AND RECOMMENDATIONS FOR FUTURE WORK

6.1 Conclusions

Potential advances in push-broom hyperspectral scanners and GNSS/INS position and orientation systems will lead to improved geospatial products only after accurate estimation of the mounting parameters relating the different sensors. Due to the widespread popularity of low-cost UAVs and the demands of non-traditional applications such as agricultural management, there is pressing need for reliable and practical estimation of the mounting parameters, in general, and boresight angles, in particular, relating the GNSS/INS unit to the scanner coordinate systems.

To ensure reliable/practical estimation of the boresight angles, this research started with a bias impact analysis to derive the optimal/minimal flight and control/tie point configuration for the estimation of the boresight angles. The conceptual basis of the bias impact analysis is deriving the flight configuration that maximizes the impact of biases in the boresight angles while ensuring the sufficiency of the flight and control/tie point configuration to avoid any potential correlation among the sought after parameters. More specifically, the analysis has shown that the optimal/minimal flight and control/tie point configuration should encompass: 1) flight lines in opposite and/or parallel directions as well as 2) GCPs or tie points that are laterally displaced from the flight lines.

The research then proceeds by introducing different calibration strategies. The first approach is an approximate one and uses tie points in overlapping scenes to estimate the boresight angles after making some assumptions regarding the flight trajectory and topography of the covered area (namely, vertical imagery over relatively flat terrain). The other two approaches are rigorous with one using GCPs while the other relying on tie points. The GCP-based rigorous approach aims at minimizing the differences between the projected object points onto the image space and the

observed image points for the used GCPs (i.e., enforcing the collinearity principle). The tie-point-based rigorous approach aims to improve the intersection of conjugate light rays corresponding to tie points (i.e., enforcing the coplanarity principle).

To verify the feasibility of the developed strategies, real datasets collected by a Nano-Hyperspec sensor mounted on a UAV were used. The compatibility of the calibration results from different flights captured at various dates verifies the feasibility of the proposed optimal/minimal flight and control/tie point configuration as well as the proposed boresight calibration strategies. The qualitative and quantitative analyses of the experimental results proved the capability of the different strategies in improving the georeferencing accuracy of hyperspectral data with the tie-point-based rigorous strategy producing the best results. The planimetric accuracy of the derived ortho-rectified mosaics turned to be at the same level of the implemented sensor GSD. For the tie-point-based rigorous calibration, the vertical accuracy is controlled by the intersection geometry.

6.2 Recommendations for Future Work

Recommendations for future work related to the proposed methodologies are presented as follows:

(1) As mentioned in Chapter 5, all the checkerboard targets are manually identified in the original hyperspectral scenes. Future work will focus on addressing this limitation. More specifically, automated identification of GCPs/tie points in the datasets will be adopted to improve the efficiency.

(2) For the proposed calibration strategies, the interior orientation parameters of the Hyperspectral scanners are available from provided specifications. Future work will be focusing on including additional parameters, e.g., the internal characteristics of the imaging scanner to improve the boresight calibration accuracy.

(3) Finally, the calibration strategy will be augmented through the incorporation of other sensors such as RGB frame cameras and LiDAR to simultaneously estimate the mounting parameters for the entire system.

REFERENCES

[1] Haboudane, D., Miller, J. R., Pattey, E., Zarco-Tejada, P. J., & Strachan, I. B. (2004). Hyperspectral vegetation indices and novel algorithms for predicting green LAI of crop canopies: Modeling and validation in the context of precision agriculture. Remote sensing of environment, 90(3), 337-352.

[2] McBratney, A., Whelan, B., Ancev, T., & Bouma, J. (2005). Future directions of precision agriculture. Precision agriculture, 6(1), 7-23.

[3] Crookston, R. K. (2006). A top 10 list of developments and issues impacting crop management and ecology during the past 50 years. Crop science, 46(5), 2253-2262.

[4] Mulla, D. J. (2013). Twenty five years of remote sensing in precision agriculture: Key advances and remaining knowledge gaps. Biosystems engineering, 114(4), 358-371.

[5] Tao, C. V., & Li, J. (Eds.). (2007). Advances in mobile mapping technology (Vol. 4). CRC Press.

[6] Habib, A., Han, Y., Xiong, W., He, F., Zhang, Z., & Crawford, M. (2016). Automated ortho-rectification of UAV-based hyperspectral data over an agricultural field using frame RGB imagery. Remote Sensing, 8(10), 796.

[7] Herwitz, S. R., Johnson, L. F., Dunagan, S. E., Higgins, R. G., Sullivan, D. V., Zheng, J., ... & Slye, R. E. (2004). Imaging from an unmanned aerial vehicle: agricultural surveillance and decision support. Computers and electronics in agriculture, 44(1), 49-61.

[8] Habib, A., Xiong, W., He, F., Yang, H. L., & Crawford, M. (2017). Improving orthorectification of UAV-based push-broom scanner imagery using derived orthophotos from frame cameras. IEEE Journal of Selected Topics in Applied Earth Observations and Remote Sensing, 10(1), 262-276.

[9] Gupta, R., & Hartley, R. I. (1997). Linear pushbroom cameras. IEEE Transactions on pattern analysis and machine intelligence, 19(9), 963-975.

[10] Verbyla, David L. Satellite remote sensing of natural resources. Vol. 4. CRC Press, 1995.

[11] Leberl, Franz, and Michael Gruber. "About frame versus push-broom aerial cameras." Microsoft Photogrammetry, Graz, Austria, Tech. Rep (2007): 1-36.

[12] Cosandier, Darren D. Generating a digital elevation model and orthomosaic from pushbroom imagery. University of Calgary, 1999.

[13] Cramer, M., Stallmann, D., & Haala, N. (2000). Direct georeferencing using GPS/inertial exterior orientations for photogrammetric applications. International Archives of Photogrammetry and Remote Sensing, 33(B3/1; PART 3), 198-205.

[14] Pfeifer, N., Glira, P., & Briese, C. (2012). Direct georeferencing with on board navigation components of light weight UAV platforms. International Archives of the Photogrammetry, Remote Sensing and Spatial Information Sciences, 39, 487-492.

[15] Elsharkawy, A. S., & Habib, A. F. (2016). Error analysis for the airborne direct georeferincing technique. ISPRS-International Archives of the Photogrammetry, Remote Sensing and Spatial Information Sciences, 1213-1219.

[16] Skaloud, J., & Lichti, D. (2006). Rigorous approach to bore-sight self-calibration in airborne laser scanning. ISPRS journal of photogrammetry and remote sensing, 61(1), 47-59.

[17] Mostafa, M. M., & Schwarz, K. P. (2001). Digital image georeferencing from a multiple camera system by GPS/INS. ISPRS journal of photogrammetry and remote sensing, 56(1), 1-12.

[18] Habib, A., Kersting, A., Bang, K., & Rau, J. (2011). A novel single-step procedure for the calibration of the mounting parameters of a multi-camera terrestrial mobile mapping system. Archiwum Fotogrametrii, Kartografii i Teledetekcji, 22.

[19] Kersting, A. P., Habib, A., & Bang, K. I. (2011, January). Mounting parameters calibration of GPS/INS-assisted photogrammetric systems. In Multi-Platform/Multi-Sensor Remote Sensing and Mapping (M2RSM), 2011 International Workshop on (pp. 1-6). IEEE.

[20] Muller, R., Manfred Lehner, Rainer Muller, Peter Reinartz, Manfred Schroeder, and Beate Vollmer. "A program for direct georeferencing of airborne and spaceborne line scanner images." International Archives of Photogrammetry Remote Sensing and Spatial Information Sciences 34, no. 1 (2002): 148-153.

[21] Yeh, C. K., & Tsai, V. J. (2015). Direct georeferencing of airborne pushbroom images. Journal of the Chinese Institute of Engineers, 38(5), 653-664.

[22] Zhang, A., Hu, S., Meng, X., Yang, L., & Li, H. (2015). Toward high altitude airship ground-based boresight calibration of hyperspectral pushbroom imaging sensors. Remote Sensing, 7(12), 17297-17311.

[23] Lenz, A., Schilling, H., Perpeet, D., Wuttke, S., Gross, W., & Middelmann, W. (2014, July). Automatic in-flight boresight calibration considering topography for hyperspectral pushbroom sensors. In Geoscience and Remote Sensing Symposium (IGARSS), 2014 IEEE International (pp. 2981-2984). IEEE.

[24] Abdel-Aziz, Y. I. (1971). Direct linear transformation from comparator coordinates in close-range photogrammetry. In Proceedings American society of photogrammetry symposium on close-range photogrammetry. Falls Church (VA). American Society of Photogrammetry Symposium on Close-Range Photogrammetry., 1971 (pp. 1-19).

[25] Nano 2017. Nano-Hyperspec Imaging Sensor – Datasheet, http://www.analytik.co.uk/wp-content/uploads/2016/03/nano-hyperspec-datasheet.pdf?x29422 (Accessed 05 November 2017).

[26] SWIR 2017. Hyperspec SWIR Hyperspectral Imaging Sensor – Datasheet, https://cdn2.hubspot.net/hubfs/145999/docs/Hyperspec_SWIR_2017.pdf?t=1521827940211 (Accessed 03 March 2018).

[27] APX 2017. Trimble APX-15 UAV (V2) - Datasheet, https://www.applanix.com/downloads/products/specs/APX15_DS_NEW_0408_YW.pdf (Accessed 30 March 2018).

[28] Hyperspec III software. Hyperspec III software – Datasheet, https://www.headwallphotonics.com/hs-fs/hub/145999/file-228855366-pdf/docs/ds_hyperspec_iii_software.pdf (Accessed 31 March 2018)

VITA

Tian Zhou received the B.S degree in remote sensing from Wuhan University, Wuhan, China, in 2015. He is currently working towards M.S degree in geomatics at the Lyles school of Civil Engineering at Purdue University, West Lafayette, IN, USA. His research interests include sensor calibration, 3D reconstruction from UAV-based imagery, and LiDAR point cloud processing.